

The Effect of Nucleation on the Quality of

MBE-ZnSe/III-V Heterostructures

by

Emily L. Warlick

Submitted to the Department of Electrical Engineering and Computer Science
in Partial Fulfillment of the Requirements for the Degrees of Bachelor of Science in
Electrical Engineering and Computer Science
and Master of Engineering in Electrical Engineering and Computer Science
at the Massachusetts Institute of Technology

December 16, 1996

Copyright 1996 Emily L. Warlick. All rights reserved.

The author hereby grants to M.I.T. permission to reproduce and
distribute publicly paper and electronic copies of this thesis
and to grant others the right to do so.

Author _____
Department of Electrical Engineering and Computer Science
December 16, 1996

Certified by _____
Leslie A. Kolodziejski
Thesis Supervisor

Accepted by _____
F. R. Morgenthaler
Chairman, Department Committee on Graduate Theses

The Effect of Nucleation on the Quality of
MBE-ZnSe/III-V Heterostructures

by

Emily L. Warlick

Submitted to the
Department Of Electrical Engineering and Computer Science

December 16, 1996

In Partial Fulfillment of the Requirements for the Degree of
Bachelor of Science in Computer Science and Electrical Engineering
and Master of Engineering in Electrical Engineering an Computer Science

ABSTRACT

ZnSe-based II-VI semiconductors represent an area of intense research, due to their promise as blue emitters for high-density optical storage systems and a range of other applications. The state-of-the-art ZnSe-based injection laser diodes that have been demonstrated to date are primarily pseudomorphic structures grown on GaAs substrates with GaAs epitaxial buffer layers. Recent electrical degradation studies have led to a growing consensus that defects arising from the ZnSe/GaAs interface presently play the limiting role in the lifetime performance of these devices. Various reports have also suggested that different nucleation procedures can lead to significant changes in the structural properties of the ZnSe overlayer. In this study, we have examined the effects of the GaAs surface reconstruction and the use of Zn or Se pre-exposure on the resultant defect densities observed in 1 μm ZnSe films grown by molecular beam epitaxy.

In order to examine the role of lattice-mismatch on the ZnSe defect density, we have also studied ZnSe grown on lattice-matched novel buffer layers of (In,Ga,Al)P on GaAs substrates. It is possible to grade the lattice constant of the buffer layer from that of GaAs to that of ZnSe. The study of these buffer layers is further motivated by their use as a p-type ohmic contact to a p-type ZnSe overlayer. We have also studied defect generation in ZnSe epilayers grown on relaxed graded buffer layers of (In,Ga)P with the phosphide surface capped with 8 monolayers of GaAs. In this manner, surface chemistry is removed as a variable while achieving a buffer layer that is lattice-matched to ZnSe. These studies have indicated that growth of ZnSe on (2x4)-reconstructed GaAs results in a defect density significantly lower than for growth of ZnSe on c(4x4)-reconstructed GaAs.

Thesis Supervisor: Leslie Kolodziejcki

Title: Associate Professor of Electrical Engineering and Computer Science

Acknowledgements

I could not have completed this research in its present state without the support of a handful of people:

- Professor Leslie Kolodziejski, for providing me with the opportunity to study this exciting area of semiconductor development, and for her unending guidance, encouragement, and support.

- Dr. Gale Petrich for helping me to learn how to run both the III-V and the II-VI systems, for always being willing to sit in the lab when I went to class, and for teaching me the difference between the east and west coast swings.

- Dr. Easen Ho for so patiently teaching me how to run the II-VI MBE chamber and for helping to get my research off to a terrific start.

- Jody House for the TEM analysis of a large number of my samples.

- Professor Fitzgerald for helpful discussions relating to semiconductor defects.

- Angela Odoardi-Mickunus for satisfying my need to talk about veggies on a regular basis and for her kindness and compassion.

- Amy Duwel for the coffee breaks, the jogging, and for her support through the endless ups and downs of life in and out of the lab.

- Jeremy Milikow for taking breaks with me, particularly during the writing of this thesis.

Most of all, I would like to thank my family for supporting and encouraging my academic pursuits over the past two decades and for their full and unqualified love.

Table of Contents

1. Introduction	15
1.1 Background	15
1.2 History of ZnSe	16
1.3 Alternative Materials Systems--GaN	19
1.4 Outline of Thesis	21
2. Molecular Beam Epitaxy of ZnSe	23
2.1 Crystal Structure of ZnSe	23
2.2 Theory of Molecular Beam Epitaxy	23
2.3 Epitaxial System and Experimental Setup	25
Growth Preparation	25
III-V GSMBE Growth	26
II-VI MBE Growth	26
2.4 N-Type Doping Using ZnCl ₂	29
2.5 P-Type Doping Using an RF Nitrogen Plasma Source	30
3. Materials Challenge	33
3.1 Lattice Match	33
3.2 (In,Ga,Al)P: Pre-Growth Calculations and Analysis	34
Lattice Constant: Calculations	34
Lattice Constant: Analysis	38
Energy Gap	40
3.3 Nucleation	41
4. Growth and Characterization	45
4.1 ZnSe/(In,Ga,Al)P/GaAs: Effect of Bandgap Match	45
4.2 ZnSe/GaAs: Effect of Nucleation	51
GaAs	51
ZnSe	54
ZnSe/GaAs	55
MBE-ZnSe/c(4x4)-reconstructed GaAs	56
MBE-ZnSe/(2x4)-reconstructed GaAs	59
Migration Enhanced Epitaxy	62
4.3 ZnSe/GaAs/(In,Ga)P: Effect of Lattice Mismatch	63
4.4 Characterization by Photoluminescence	71
5. Future Research	77

5.1 LED Structure: Design and Analysis	77
5.2 Recent Advance	78
5.3 Future Pursuits	79
<i>Appendix A: In-Situ Characterization Techniques</i>	81
A.1 Reflection High Energy Electron Diffraction	81
A.2 Auger Electron Spectroscopy	82
<i>Appendix B: Structural Characterization</i>	83
B.1 X-Ray Double Crystal Diffraction	83
B.2 Photoluminescence	84
B.3 Cathodoluminescence	84
B.4 Atomic Force Microscopy	85
B.5 Transmission Electron Microscopy	85
B.6 Etch Pitting	86
<i>Appendix C: Electrical Characterization</i>	89
C.1 ZnSe pn-junction Diodes	89
C.2 ZnSe Light-Emitting Diodes	89
C.3 I-V Measurements	90
<i>Bibliography</i>	93

List of Figures

Figure 1.1: Bandgap versus lattice constant for II-VI and III-V binary materials. The ellipse in the middle indicates the spectral sensitivity of the human eye. The edge of red light detection is at 1.8 eV; the edge of blue light is at 3.1 eV.

Figure 1.2: Timeline of progress of II-VI based light emitting diodes.

Figure 2.1: Schematic diagram of the MIT heteroepitaxial system: III-V GSMBE chamber, II-VI MBE chamber, and a UHV transfer chamber for II-VI/III-V growth.

Figure 2.2: [Cl] versus ZnCl₂ effusion cell temperature, as determined by SIMS analysis.

Figure 2.3: Incorporated nitrogen concentration, [N], as a function of RF Power * Gas Pressure (reproduced from ref. 22).

Figure 3.1: An epilayer grown on a lattice-matched substrate. The in-plane lattice constants of the two materials are equal.

Figure 3.2: A relaxed epilayer on a lattice-mismatched epilayer. The in-plane lattice constant of the epilayer is larger than that of the substrate.

Figure 3.3: A pseudomorphic epilayer on a lattice-mismatched epilayer. The in-plane lattice constant of the epilayer is larger than that of the substrate, so, for thin layers, the lattice is strained to match the substrate.

Figure 3.4: Lattice constant as a function of composition (reproduced from ref. 11).

Figure 3.5a: RHEED oscillations during growth of GaAs. $\tau_{\text{Ga}}^{-1} = 0.596 \mu\text{m/hr}$.

Figure 3.5b: RHEED oscillations during growth of InGaP. $\tau_{\text{InGa}}^{-1} = 1.113 \mu\text{m/hr}$

Figure 3.6a: X-Ray double crystal rocking curve of 1 μm ZnSe grown on a GaAs buffer layer. ZnSe peak at -2750 sec, GaAs peak at -2400 sec. $\text{FWHM}_{\text{GaAs}} = 37 \text{ sec}$.

Figure 3.6b: X-Ray double crystal rocking curve of 1 μm ZnSe grown on a graded InGaP buffer layer. ZnSe peak at -4000 sec, GaAs peak at -3200 sec. $\text{FWHM}_{\text{GaAs}} = 90 \text{ sec}$.

Figure 3.7: Energy bandgap (eV) versus lattice constant (a) for the (In,Ga,Al)P III-V material group and for GaAs and ZnSe.

Figure 3.8a: Schematic of a pair of stacking faults surrounded by Shockley dislocations nucleated at the GaAs/ZnSe interface.

Figure 3.8b: Schematic of the plan view TEM image of a pair of stacking faults surrounded by Shockley dislocations nucleated at the GaAs/ZnSe interface.

Figure 3.9: Schematic of plan view TEM image of misfit dislocations in a ZnSe/GaAs structure.

Figure 3.10: Threading dislocation formed along a slip plane (dashed line).

Figure 4.1: Theoretical valence band offsets for the GaAs/ZnSe structure and the GaAs/(In,Ga,Al)P/ZnSe structure. GaAs/ZnSe has a 0.96 eV valence band discontinuity; InAlP/ZnSe has a 0.35 eV valence band discontinuity.

Figure 4.2: Photoluminescence scans of 1 μ m ZnSe grown on InAlP. The top figure shows the scan for pseudomorphic ZnSe (not relaxed). The bottom figure shows the scan for relaxed ZnSe with a deep level centered around 2.3 eV.

Figure 4.3a: CL of Sample #2--1 μ m ZnSe on 4 μ m relaxed graded layer of (In,Ga)P. T = 300K; Mag = 1700x.

Figure 4.3b: CL of Sample #3--1 μ m ZnSe on 4 μ m relaxed stepped layer of (In,Al)P. T = 300K; Mag = 1700x.

Figure 4.3c: CL of Sample #5--1 μ m ZnSe on 4 μ m relaxed graded layer of (In,Ga,Al)P. T = 300K; Mag = 1700x.

Figure 4.4: Atomic force micrograph of 1 μ m ZnSe film grown by MBE on 4 μ m linearly graded (In,Ga,Al)P buffer layer. The mean roughness value over a 500 nm x 500 nm area was 4Å.

Figure 4.5a: RHEED pattern of (2x4)-reconstructed GaAs at growth temperature (T_c=640°C).

Figure 4.5b: RHEED pattern of (2x4)-reconstructed GaAs before transfer (T_c=270°C).

Figure 4.6a: Top view and side view of c(4x4)-reconstructed GaAs (100% arsine surface coverage). (reproduced from ref. 38)

Figure 4.6b: Top view and side view of (2x4)-reconstructed GaAs (75% arsine surface coverage). (reproduced from ref. 38)

Figure 4.7: Surface configurations for ZnSe on GaAs. The trend in band offsets is based on theoretical analysis.

Figure 4.8: (a) MBE-ZnSe/c(4x4)-reconstructed GaAs with Zn and Se shutters opened simultaneously; (b) MBE-ZnSe/c(4x4)-reconstructed GaAs with a 2 minute Zn pre-exposure; (c) MBE-ZnSe/c(4x4)-reconstructed GaAs with 1 min Se pre-exposure.

Figure 4.9: Atomic force micrograph of 1 μm ZnSe film grown by MBE on a Zn pre-exposed c(4x4)-reconstructed GaAs buffer layer (sample 7).

Figure 4.10: Room temperature CL image of MBE-ZnSe/(2x4)-reconstructed GaAs with a 2 min Zn pre-exposure (sample 9); Mag=1700x.

Figure 4.11: Atomic force micrograph of 1 μm ZnSe film grown by MBE on a Zn pre-exposed (2x4)-reconstructed GaAs buffer layer (sample 9).

Figure 4.12a: 1 μm ZnSe grown on c(4x4)-reconstructed GaAs with a one minute Zn pre-exposure followed by ten cycles of MEE (cycle = 3 sec Se, 2 sec delay, 3 sec Zn) at 260°C and 24 more cycles of MEE while ramping to the growth temperature.

Figure 4.12b: 1 μm ZnSe grown on (2x4)-reconstructed GaAs with a one minute Zn pre-exposure followed by ten cycles of MEE (cycle = 3 sec Se, 2 sec delay, 3 sec Zn) at 260°C and 24 more cycles of MEE while ramping to the growth temperature.

Figure 4.13: Schematic of growths used to study the effect of lattice-mismatch.

Figure 4.14a: TEM micrograph of sample 9 (1 μm ZnSe on (2x4)-reconstructed GaAs). Micrograph is about 4 μm wide. TEM courtesy of Jody House.

Figure 4.14b: TEM micrograph of sample 11 (1 μm ZnSe on (2x4)-reconstructed GaAs on a graded (In,Ga)P buffer layer). Micrograph is about 2.5 μm wide. TEM courtesy of Jody House.

Figure 4.15a: Room temperature CL of 1 μm ZnSe film grown by MBE on 4 μm linearly graded (In,Ga)P buffer layer with a two minute Zn-exposed eight monolayer c(4x4)-reconstructed GaAs layer between the (In,Ga)P and ZnSe (sample 10). Mag = 1700x.

Figure 4.15b: EPD photograph of 1 μm ZnSe film grown by MBE on 4 μm linearly graded (In,Ga)P buffer layer with a two minute Zn-exposed eight monolayer c(4x4)-reconstructed GaAs layer between the (In,Ga)P and ZnSe (sample 10). Mag=400x. EPD=3x10⁷ cm⁻².

Figure 4.16a: Room temperature CL of 1 μm ZnSe film grown by MBE on 4 μm linearly graded (In,Ga)P buffer layer with a two minute Zn-exposed eight monolayer (2x4)-reconstructed GaAs layer between the (In,Ga)P and ZnSe (sample 11). Mag=1700x.

Figure 4.16b: EPD photograph of 1 μm ZnSe film grown by MBE on 4 μm linearly graded (In,Ga)P buffer layer with a two minute Zn-exposed eight monolayer (2x4)-reconstructed GaAs layer between the (In,Ga)P and ZnSe (sample 11). Mag=400x. EPD=1.6x10⁶ cm⁻².

Figure 4.17a: Atomic force micrograph of 1 μ m ZnSe film grown by MBE on 4 μ m linearly graded (In,Ga)P buffer layer with a Zn-exposed 8 monolayer c(4x4)-reconstructed GaAs layer between the (In,Ga)P and the ZnSe (sample 10). $R_a = 7\text{\AA}$.

Figure 4.17b: Atomic force micrograph of 1 μ m ZnSe film grown by MBE on 4 μ m linearly graded (In,Ga)P buffer layer with a Zn-exposed 8 monolayer (2x4)-reconstructed GaAs layer between the (In,Ga)P and the ZnSe (sample 11). $R_a = 3\text{\AA}$.

Figure 4.18a: 10K photoluminescence scan of 1 μ m ZnSe grown with a Zn pre-exposure on c(4x4)-reconstructed GaAs (sample 7).

Figure 4.18b: 10K photoluminescence scan of 1 μ m ZnSe grown with a Zn pre-exposure on (2x4)-reconstructed GaAs (sample 9).

Figure 4.19a: 10K photoluminescence scan of 1 μ m ZnSe grown with a Zn pre-exposure on a graded (In,Ga)P buffer layer with a c(4x4)-reconstructed GaAs cap (sample 10).

Figure 4.19b: 10K photoluminescence scan of 1 μ m ZnSe grown with a Zn pre-exposure on a graded (In,Ga)P buffer layer with a (2x4)-reconstructed GaAs cap (sample 11).

Figure 5.1: Schematic of pn diode showing doping and composition of each layer.

Figure 5.2: Current versus applied voltage characteristic of a ZnSe p-n diode consisting of ZnSe grown on c(4x4)-reconstructed GaAs.

Figure A.1: ZnSe surface reconstructions for the Se-rich and Zn-rich cases.

Figure A.2: Schematic of the theory of auger electron emission.

Figure B.1: Primary features seen in PL spectra of ZnSe epilayers.

Figure B.2: Image of etch pits in sample of 1 μ m ZnSe/GaAs. One second etch with 1% bromine solution of bromine-methanol—250nm. EPD = $9 \times 10^7 \text{ cm}^{-2}$.

Figure C.1: Injection of electrons and holes under forward bias with $N_D \gg N_A$.

Figure C.2: Theoretical ZnSe LED with $N_D \gg N_A$.

Figure C.3: General form of a current versus voltage characteristic for a p-n junction diode.

List of Tables

Table 4.1: (In,Ga,Al)P layers used as buffers for 1 μ m ZnSe epilayers.

Table 4.2: Pre-exposures used in MBE-ZnSe/c(4x4)-reconstructed growths.

Table 4.3: Correlation between Y_0 and deep level transitions measured by 10K PL, and dislocation density, DD (cm⁻²), measured by CL and EPD, of samples 7 and 9.

Table 4.4: Correlation between Y_0 and deep level transitions measured by 10K PL, and dislocation density, DD (cm⁻²), measured by CL and EPD, of samples 10 and 11.

Table C.1: Details of evaporation and thermal annealing for contacts to n-type and p-type GaAs and to n-type ZnSe.

Chapter 1: Introduction

1.1 Introduction

Over the past ten years, intense research has resulted in fantastic breakthroughs in the area of II-VI compound semiconductor blue/green light emitters. The large bandgap of the II-VI semiconductors allows for the possibility of developing blue light emitting devices. The wide direct room temperature bandgap of ZnSe (2.67 eV) makes ZnSe-based devices ideal for use in short wavelength light emitters. With a wavelength approximately one-half of the wavelength of the present lasers that are used in compact-disc players, ZnSe-based laser diodes will at least quadruple data density. ZnSe light-emitting diodes will also provide the missing blue color necessary for full three color displays, which are presently satisfied to a limited extent by GaN blue light emitting diodes.

Figure 1.1 shows the III-V and II-VI material systems. The large number of materials available for incorporation into ZnSe growth, most notably the group II materials Be, Mg, and Cd, and the group VI materials S and Te, allow for the growth of a highly confining active region in ZnSe-based light emitters. Such a region can significantly improve the external quantum efficiency of the diode and can yield a narrow emission spectra, resulting in sharper color output.

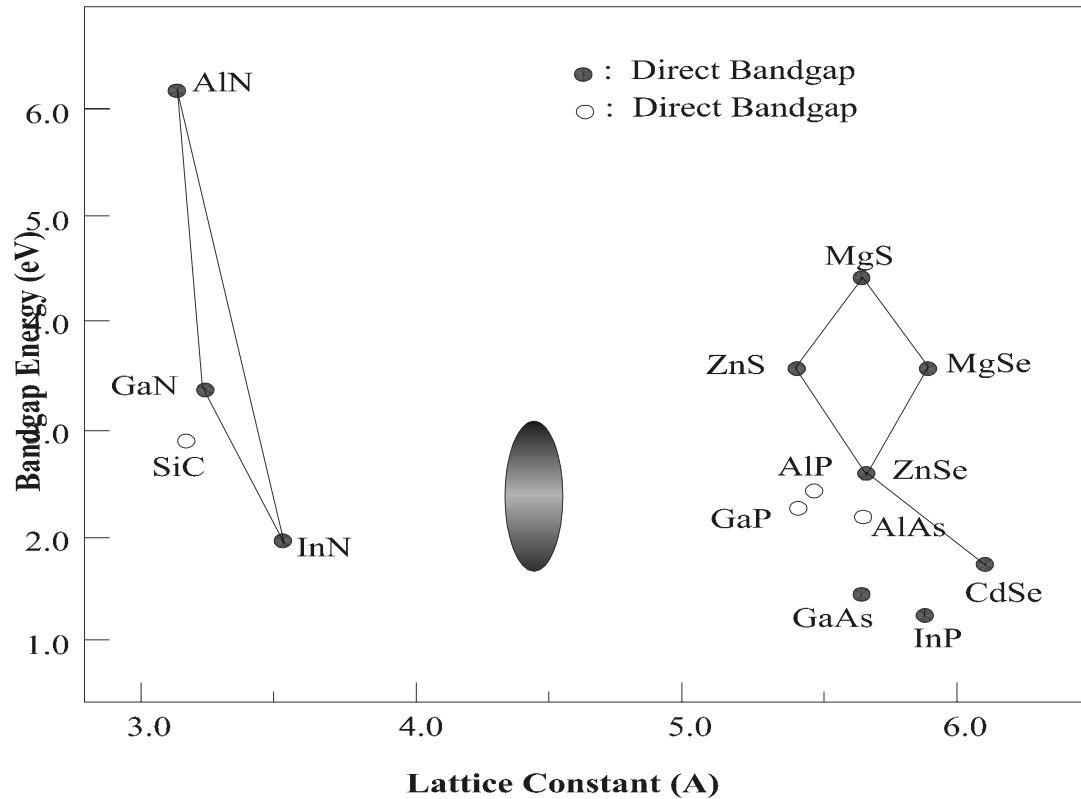


Figure 1.1: Bandgap versus lattice constant diagram for II-VI and III-V binary materials. The ellipse in the middle indicates the spectral sensitivity of the human eye. The edge of red light detection is at 1.8 eV; the edge of blue light is at 3.1 eV.

1.2 History of ZnSe

ZnSe-based laser diodes have a long, interesting history. Research of semiconductor materials began about thirty years ago. Numerous difficulties in II-VI semiconductors, however, caused III-V semiconductor research to surge ahead of the II-VI research in the late 1970s, when the research of II-VI semiconductors was largely relegated to academia.

In the early 1980s, research was aimed at determining the ideal growth technique for epitaxial II-VI films. Several techniques were pursued, most notably molecular beam

epitaxy (MBE) and metalorganic chemical vapor deposition (MOCVD). By 1985, it was evident that MBE offered the greatest promise for high-quality ZnSe epilayers [1].

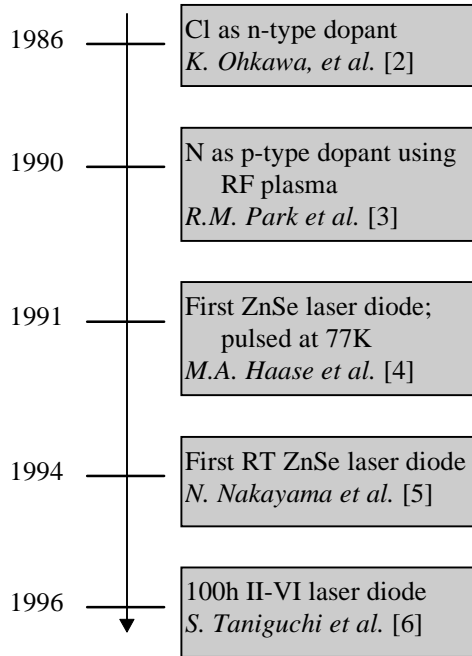


Figure 1.2: Timeline of progress of II-VI based light emitting devices.

Around this time, a great deal of progress was made in terms of minimizing defect density, reducing resistivity, and generally improving the material quality of the MBE-grown ZnSe. Simultaneously, many groups were searching for potential n- and p-type dopants for ZnSe. The problem of n-type doping of ZnSe proved to be much easier to solve. Initially, Ga was used as the n-type dopant [1]. The maximum carrier concentration obtained by Ga doping was $5 \times 10^{17} \text{ cm}^{-3}$. In 1986, a group at Matsushita Electric in Japan grew Cl-doped ZnSe by MBE using ZnCl_2 as a doping source [2]. At the dopant cell temperature of $T_{\text{Cl}}=250^\circ\text{C}$, the resultant carrier concentration reached about $1 \times 10^{19} \text{ cm}^{-3}$.

Several years of research elapsed before a p-type doping source was discovered. Early p-type doping utilized Li, but the high diffusivity of Li resulted in a maximum carrier concentration of only $1 \times 10^{17} \text{ cm}^{-3}$. Nitrogen-doping was also studied as a candidate because it is a shallow level acceptor and has a high solubility limit in ZnSe. In 1990, Park et al. discovered a novel means of N doping whereby active nitrogen was produced by a plasma discharge [3]. By these means, p-type doping of ZnSe of up to $1 \times 10^{18} \text{ cm}^{-3}$ became immediately possible.

Thus, by 1991, the materials necessary to grow a ZnSe p-n junction diode was available. A few months later, a group at 3M Company announced the fabrication of the first II-VI laser diode [5]. The device emitted coherent light at a wavelength of 490 nm from a ZnSe-based structure under pulsed current injection at 77 K. Shortly thereafter, similar results were announced by a group of Brown/Purdue University researchers [6].

After this breakthrough, new problems arose, causing long delays before room temperature continuous wave (CW) operation was announced by the Sony Corporation in 1994 [7]. This delay was primarily due to the difficulty of obtaining an ohmic contact to p-type ZnSe. Initial contacts utilized Au, but they exhibited high contact resistance. The first room temperature CW operation of a II-VI laser diode used Pd/Pt/Au ohmic metals to reduce the operating voltage of the device. Au is required as a contact to external devices and the Pt acts as a barrier between the Pd and Au layers to keep the Au from diffusing into the device.

The present thrust of the II-VI saga is to increase the lifetime of the laser diodes, primarily by decreasing the defect densities in the active region of the devices. The first room temperature (RT) diode from Sony Corp. operated for 9 seconds [7]. In February

1996, this same group announced a lifetime of 100 hours under room temperature CW operation with a constant light output power of 1mW [8]. The defect density of this laser diode was reported to be $3 \times 10^3 \text{ cm}^{-3}$.

1.3 Alternative Materials Systems—GaN

There are, in fact, two strong contenders in the race for blue light emitting devices. Research groups are working on both II-VI ZnSe-based light emitting devices and, separately, on III-V GaN-based devices.

Nichia Chemical Industries has become globally renowned since its announcement on November 29, 1993 that it had developed a bright blue, GaN-based blue LED and would soon sell the device commercially. The first single-crystal GaN material was produced at the David Sarnoff Research Center in the early 1970s [11]. Even after this breakthrough, few groups showed interest in the material, primarily due to the seemingly hopeless tasks of finding both an acceptable substrate and a p-type dopant.

Two people are primarily responsible for the progress of GaN devices. Isamu Akasaki of Meijo University has been working on GaN development since 1974. While working at Nagoya University in 1986, he was able to produce high quality GaN using an AlN buffer layer [12]. Then, in 1989, he accidentally discovered that Mg can be used as a p-type dopant for GaN [13].

Shuji Nakamura began working at Nichia Chemical Industries in 1975 and began his search for a blue light source in 1988. To avoid patent problems with Akasaki, Nakamura used GaN as a buffer layer, and found that he was able to grow high quality GaN with very good electrical properties. Nakamura was able to improve Akasaki's p-

type doping technique and, in March 1991, Nakamura produced the first blue light emitter [14]. The light output of this early device was very low. Two and a half years later, Nichia publicly announced 1000 mcd blue LEDs. Nakamura is now working to develop a blue GaN laser.

Since Nichia's public announcement, the number of groups researching GaN-based devices has multiplied dramatically. Neither ZnSe nor GaN-based devices presently has a clear advantage. The greatest problem with GaN devices is the lack of a lattice-matched substrate, which results in a very high defect density in the devices. Most GaN growth is performed on Al₂O₃ (sapphire) substrates which have a lattice constant 14% larger than GaN and a thermal expansion coefficient almost twice as large as that of GaN. In order to grow high quality devices on these substrates, thick (several μm) buffer layers of AlN or GaN are grown. Even so, the Nichia blue GaN LEDs have dislocation densities in excess of 10¹⁰ cm⁻² [15].

Since the Fermi level of the GaN is not pinned, dislocations have a smaller or even nonexistent effect on GaN surface properties, and thus do not seem to degrade LED lifetime by acting as non-radiative recombination sites, as occurs in other III-V materials and in ZnSe-based LEDs. Many people still believe that the GaN dislocation density will have to be dramatically reduced before a GaN laser diode can be developed. The high GaN defect densities have led some researchers to consider growth on other substrates, most notably SiC, which has a closer lattice-match to GaN. Another possibility is ZnO, which has an even closer lattice match, but ZnO substrates are not yet commercially available.

Presently, the maximum lifetime of a II-VI blue laser diode at room temperature CW is just slightly above 100 hours [6]. The maximum lifetime of a III-V GaN laser is about one hour [11]. LEDs of both materials have lifetimes of tens of thousands of hours [16,17].

Only time will tell which material system will prove to be best for blue laser operation. (see references 9, 10, and 11 for further reading)

1.4 Outline of Thesis

The primary limitation of II-VI-based laser diode structures is their high defect densities, which leads to rapid degradation of devices. The long-term goal of this research is to produce ZnSe-based LEDs using novel III-V buffer layers with bandgap energies between those of ZnSe and GaAs to act as hole-injection layers. The shorter-term goal of the research is to optimize the growth of MBE-ZnSe on such III-V buffer layers, and to eventually apply the technique to the growth of ZnSe-based LED structures. A recent report stated that the density of the lifetime-limiting extended defects in a ZnSe epilayer to be as low as $1 \times 10^5 \text{ cm}^{-2}$ [18].

The growth technique of choice for the III-V buffer layers is gas source molecular beam epitaxy (GSMBE) and for ZnSe, the growth technique of choice is molecular beam epitaxy (MBE). These epitaxial growth processes are described in detail in Chapter 2.

The III-V buffer layers have a significant impact on the growth quality of the ZnSe overlayer. Pre-growth calculations and a discussion on the lattice match and the band gap energies are given in Chapter 3.

Chapter 4 describes the growth characterization by the analysis of defect density and presents the primary results of this research. Cathodoluminescence (CL) imaging was the most instructive characterization technique used, providing clear proof of a reduction in defect density of ZnSe epilayers grown on III-V buffer layers with highly controlled surface stoichiometry at the II-VI/III-V heterointerface.

The characterization techniques are discussed in the Appendix. These techniques, both structural and electrical, were used to determine the optimum growth conditions for use in future research.

Chapter 2: Molecular Beam Epitaxy of ZnSe

2.1 Crystal Structure of ZnSe

ZnSe is an ionic compound. Like most II-VI compounds, it crystallizes in the zincblende structure. This structure is similar to the diamond lattice, which consists of two interpenetrating face-centered cubic Bravais lattices or a single FCC Bravais lattice with two atoms associated with a single lattice point. In the zincblende structure, the atoms in the center of the unit cell are different from those at the corners and on the faces. ZnSe consists of Zn atoms in the interior of the unit cell and Se atoms on the edges, such that four Zn atoms tetrahedrally surround one Se atom and four Se atoms tetrahedrally surround one Zn atom. The lattice constant, or side length of the unit cell, of ZnSe is 5.6676 Å.

2.2 Theory of Molecular Beam Epitaxy

The past two decades have been an era of large-scale development of semiconductor heterostructures. In the simplest sense, a heterostructure consists of one semiconductor deposited on to another, chemically different, semiconductor.

In order to improve the properties of heterostructure devices, the process of epitaxial growth is the subject of intense research.

Molecular Beam Epitaxy (MBE) has many advantages over other techniques, such as Liquid Phase Epitaxy (LPE). MBE allows for the growth of abrupt interfaces and

doping profiles. It also allows the epilayers' thickness to be controlled on the scale of a single monolayer.

MBE involves the thermal deposition of molecules or atoms onto a heated substrate in an ultrahigh vacuum environment.

The material needed for growth is placed in crucibles, which are in turn placed in effusion cells. The generation of a molecular beam involves heating the effusion cell to increase the vapor pressure of the material. Each effusion cell has a tantalum shutter in front of the crucible, which are used to block atoms from the substrate surface. When the shutter is opened, the molecules travel in the ultrahigh vacuum without collisions until they are deposited onto the substrate.

The flux of atoms or molecules leaving the effusion cell crucible per second is

$$F = \frac{PANA}{\sqrt{2\pi MRT}} = 3.51 \times 10^{22} \frac{PA}{\sqrt{MT}} \text{ molecules / s [19]}$$

where M = molecular weight, Na = Avagadro's number, P = pressure (torr) inside the effusion cell, R = gas constant, T (K) = temperature of the cell, A = area of the aperture. This flux must be carefully monitored. The ratio of the flux of the group II element to that of the group VI element plays a significant role in the growth rate of the compound semiconductor as well as in the quality of the epitaxy. This ratio is the flux ratio. For ZnSe, a high flux ratio causes zinc atoms to hinder the surface diffusion of the selenium adatoms [20].

The ability of a MBE system to produce uniform epitaxial growth is highly dependent upon its geometry. The source-to-substrate distance must be sufficiently short that molecules do not collide with other molecules of a different species before reaching the substrate surface. Specifically, the mean free path of the molecules must be longer

than the source-to-substrate distance. Another source of surface non-uniformity is due to the placement of effusion cells. Because of the nature of the process, it is not possible to place effusion cells containing two different materials at precisely the same location. The difference in the angle between the cells and the substrate results in non-uniform deposition [21]. To minimize this effect, the substrate is rotated during growth.

2.3 Epitaxial System and Experimental Setup

Figure 2.1 schematically shows the heteroepitaxial system in use at MIT for II-VI and III-V compound semiconductor growth. An ultrahigh vacuum (UHV) chamber connects with a GSMBE III-V system (Riber CBE32P) to a MBE II-VI system (custom built with parts from Emcore). The UHV transfer chamber allows for II-VI materials to be grown on III-V buffer layers, as described in this research.

Growth Preparation

All growths were performed on full 2” epi-ready GaAs wafers from AXT Crystal, Inc. The epi-ready GaAs wafer is first placed in a molybdenum block (which is previously baked at 450°C for two hours) and loaded into the introduction chamber (see figure 2.1). The sample is then moved via a mechanical arm in the transfer chamber to a bake station where it is baked at 210°C for one hour. The baking process reduces the water and adsorbed gases from the substrate prior to its introduction into the III-V system. After the bake, the sample is moved to the III-V growth chamber.

III-V GSMBE Growth

The growth of the III-V buffer layers is performed by GSMBE. GSMBE is based on the general principles of MBE as discussed above, but utilizes gaseous sources for the group V elements. Effusion cells are used for the group III elements (In, Ga, and Al) and are heated to temperatures of 750°C to 1200°C, depending on the element. The group V elements are generated by “cracking” the hydride gases AsH₃ and PH₃. These hydrides, in conjunction with mass flow controllers (MFCs), simplifies the problem of flux control associated with the high vapor pressure elements As and P. The hydrides are thermally decomposed in a high temperature, low pressure cracker. The MFCs are used to precisely control the gas flow onto the substrate surface.

II-VI MBE Growth

In the II-VI system, a vacuum pressure of about 10⁻⁹ Torr is achieved by a combination of four pumps: ion, cryogenic, diffusion, and a titanium sublimation pump.

A reflection high energy electron diffraction (RHEED) (see appendix) screen is mounted in the center of the chamber to allow simple in-situ surface characterization. Eight 6” flange positions are available around the circumference of the reactor. Three positions are used for effusion ovens from EPI Corporation. These ovens contain elemental ultra-high purity (6N) Zn as the cation species, elemental (6N) Se as the anion species, and ZnCl₂ for Cl doping. For ZnSe growth, the Zn effusion cell is heated to about 310°C and the Se effusion cell is heated to about 190°C, which results in a flux ratio of about $F_{Zn}/F_{Se} = 0.7$, as measured by a water-cooled crystal quartz oscillator. The quartz crystal oscillator is located about 2 cm below the substrate position.

Smaller flange ports contain an optical pyrometer, a CCD camera, and viewports to assist in sample manipulation. A nitrogen plasma source from Oxford Research (LN₂-cooled CARS25) is the p-type dopant source. The nitrogen flow into the reactor is controlled by a variable leak valve. An RF power of approximately 350 W is used.

Neither Zn nor Se exhibits a unity sticking coefficient. Therefore, a unity flux ratio requires careful control of the material fluxes and the substrate temperature. Temperatures are measured simultaneously by a thermocouple and by a pyrometer. The substrate temperature was calibrated with the Au-Ge eutectic transition (356°C). The pyrometer emissivity was adjusted at the transition to yield an accurate reading. The offset of the thermocouple at this point was noted. All growth temperatures in this thesis refer to that of the calibrated pyrometer. Oscillations of the pyrometer temperature during growth provide a convenient and accurate technique for monitoring the ZnSe thickness.

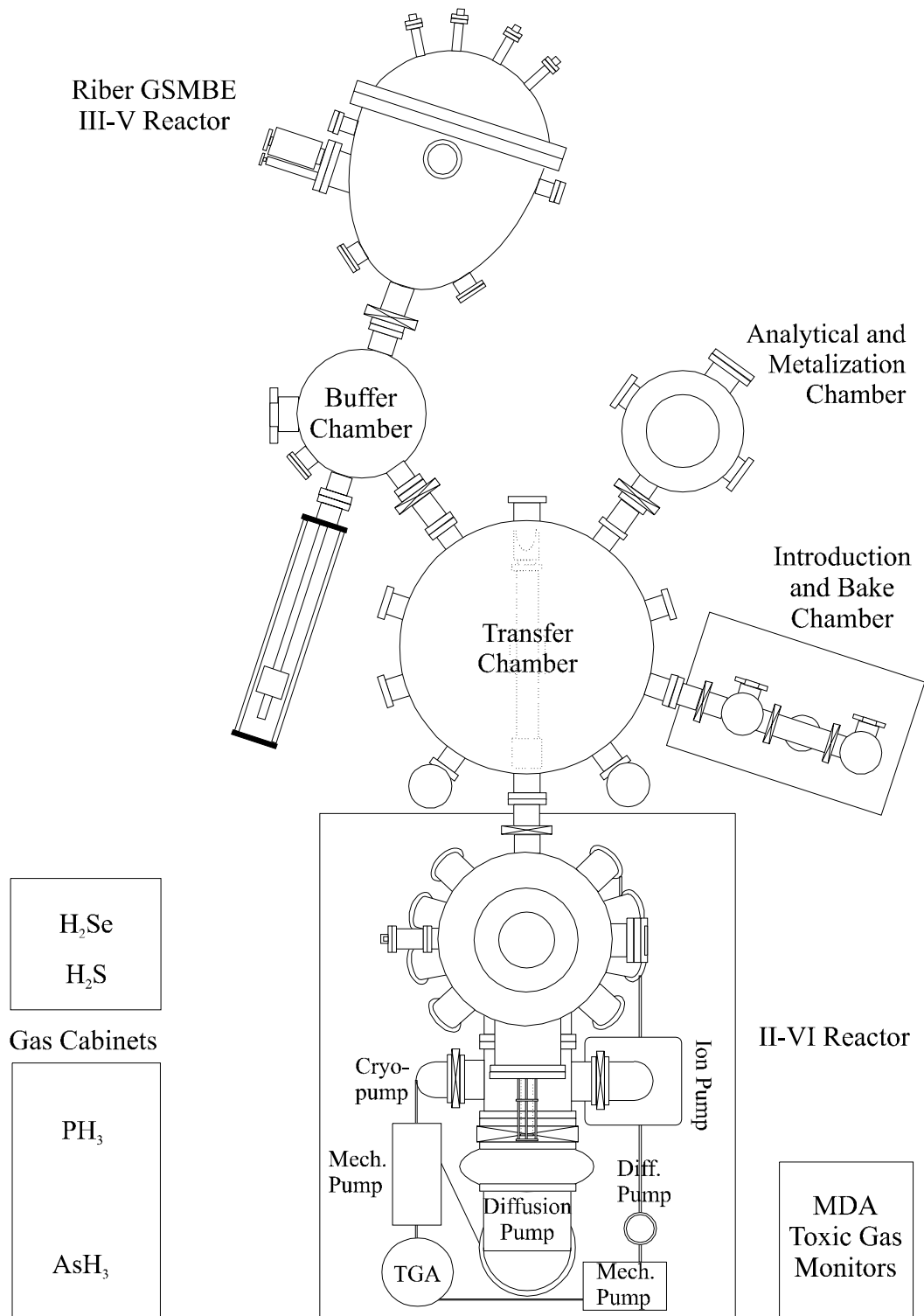


Figure 2.1: Schematic diagram of the MIT heteroepitaxial system: III-V GSMBE chamber, II-VI MBE chamber, and a UHV transfer chamber for II-VI/III-V growth.

2.4 N-Type Doping Using ZnCl₂

As discussed previously, shallow n-type doping of ZnSe using ZnCl₂ has been in use since 1986 when a carrier concentration of $1 \times 10^{19} \text{ cm}^{-3}$ was achieved by heating a ZnCl₂ effusion cell to 250°C during growth. In our laboratory, solid, anhydrous ZnCl₂ is used in an effusion cell to achieve n-type doping in ZnSe by MBE. The effect of the ZnCl₂ cell temperature on the [Cl] concentration, as shown in figure 2.2, was determined by secondary ion mass spectroscopy (SIMS) [22], which was performed by Charles Evans and Associates.

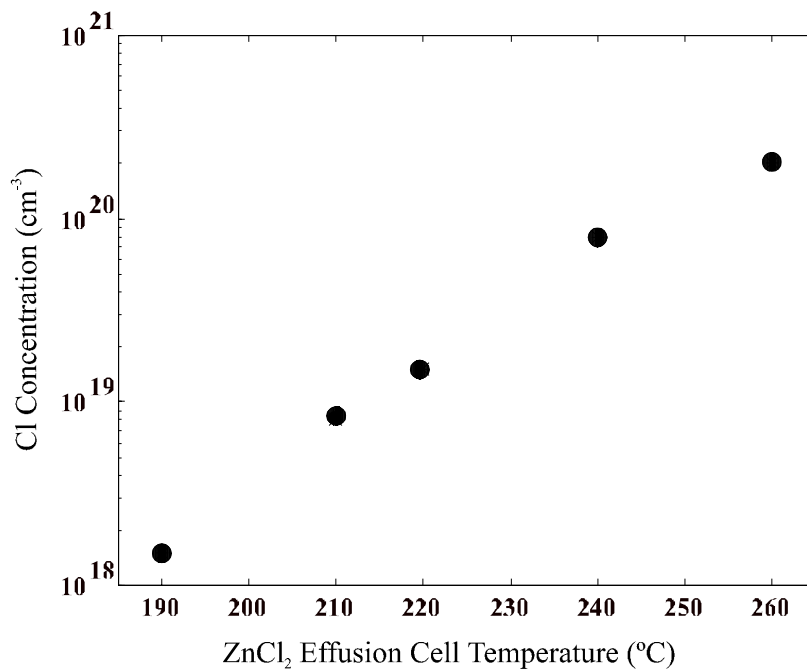


Figure 2.2: [Cl] versus ZnCl₂ effusion cell temperature, as determined by SIMS analysis.

As seen in the semilogarithmic plot, with other parameters constant, chlorine concentration has an exponential dependence on the ZnCl₂ effusion cell temperature.

2.5 P-Type Doping Using an RF Nitrogen Plasma Source

P-type doping of ZnSe-based materials proved to be much more difficult than n-type doping. The problems encountered in realizing low-resistivity p-type ZnSe films were due to self-compensation of acceptor impurities. For many years, this self-compensation was explained as the result of doping-activated native defects [23]. It is now thought that the mechanism for self-compensation of acceptors in ZnSe is the large atomic relaxation in the vicinity of acceptor impurities which affects the electrical properties of the material [24]. The realization of high-concentration p-type doping up to the 10^{18} cm^{-3} range using nitrogen was made independently by Park *et al.* [3] and Ohkawa *et al* [25].

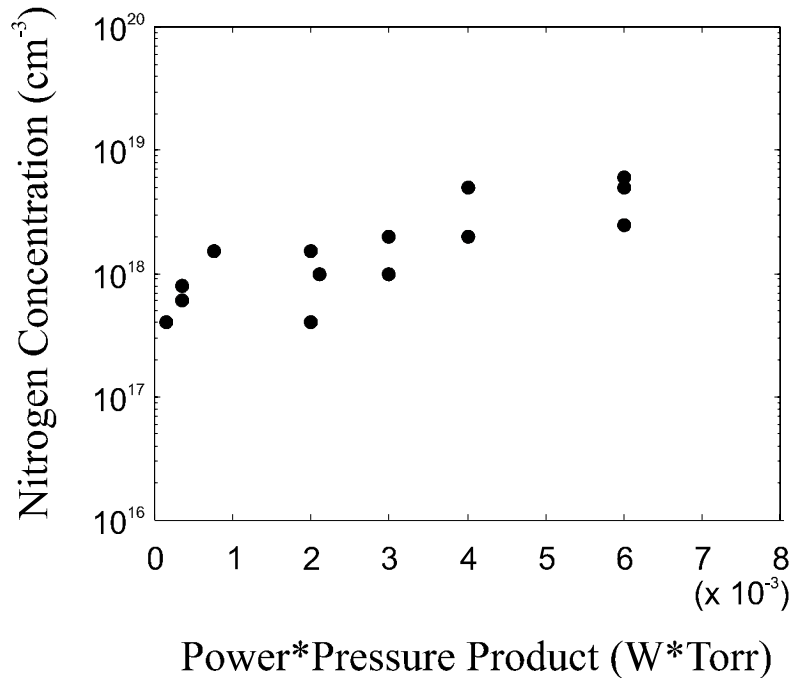


Figure 2.3: Incorporated nitrogen concentration, [N], as a function of RF Power * Gas Pressure (reproduced from ref. 22).

The N concentration in ZnSe increases with both increasing RF power [26] and increasing aperture area of the plasma cell [27]. For the experiments described in this thesis, the doping concentration was determined from SIMS analysis of previously grown samples with differing RF power and aperture configurations. This data is reproduced in figure 2.3 (plot from ref. 17).

Chapter 3: Materials Design

3.1 Lattice Match

All things equal, growth of a lattice-matched layer is of higher quality than one that is lattice-mismatched. When the lattice constant of two semiconductors are matched, and the nucleation procedure is optimized, the epilayer can grow very smoothly, as shown in figure 3.1 below.

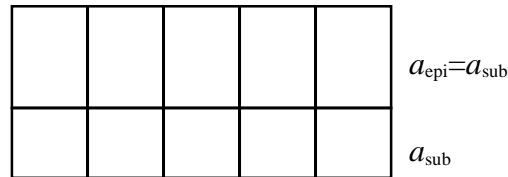


Figure 3.1: An epilayer grown on a lattice-matched substrate. The in-plane lattice constants of the two materials are equal.

Materials with different in-plane lattice constants behave differently. The inherent strain in a thick epilayer is released as misfit dislocations. However, since releasing strain as misfit dislocations requires energy, thin epilayers (pseudomorphic) will be totally elastically strained. At the critical thickness, the strain energy released by misfit dislocations equals the energy required to form the misfits. Beyond this critical thickness, misfit dislocations form, relaxing the strain in the layer.

The critical thickness is given by

$$h_c = 4\alpha b/f, \quad b \text{ is the Burgers vector of the defect, } \alpha \text{ is a geometrical factor, } f \text{ is the lattice-mismatch.}$$

Figures 3.2 and 3.3 show a relaxed and a pseudomorphic epilayer grown on a lattice-mismatched substrate.

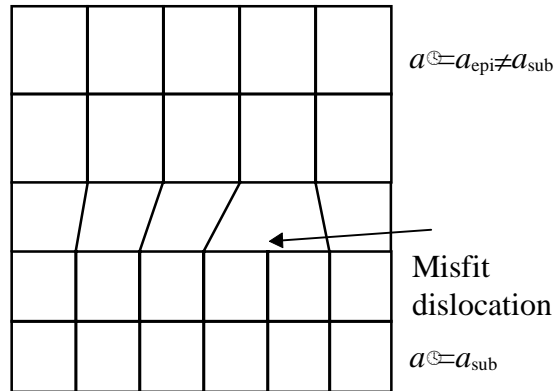


Figure 3.2: A relaxed epilayer on a substrate. The in-plane lattice constant of the epilayer is larger than that of the substrate.

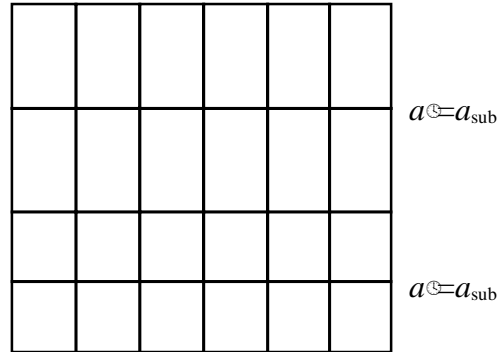


Figure 3.3: A pseudomorphic epilayer on a lattice-mismatched epilayer. The in-plane lattice constant of the epilayer is larger than that of the substrate, so, for thin layers, the lattice is strained to match the substrate.

3.2 (In,Ga,Al)P: Pre-Growth Calculations and Analysis

Lattice Constant: Calculations

Due to the formation of misfit dislocations at the ZnSe/GaAs interface as a result of the 0.27% lattice mismatch [28], a series of samples were grown with an additional InGaP buffer layer inserted between the GaAs and the ZnSe. With the proper composition, InGaP can be lattice matched to both GaAs and ZnSe.

By lattice-matching the InGaP buffer layer to the underlying GaAs buffer layer and to the overlying ZnSe layer, misfit dislocation in the ZnSe layer can be dramatically reduced. To achieve the high degree of lattice match necessary, the initial InGaP must be grown with the same in-plane lattice constant as GaAs, namely 5.653Å and the final monolayers of InGaP must be grown with the same in-plane lattice constant as ZnSe, namely 5.668Å.

The linear variation in lattice constant with respect to composition for such a ternary alloy is described by Vegard's Law. For $\text{In}_{1-x}\text{Ga}_x\text{P}$, this relation is given by:

$$a = 5.869 - 0.418x$$

This relationship between lattice constant and mole fraction is shown in figure 3.4.

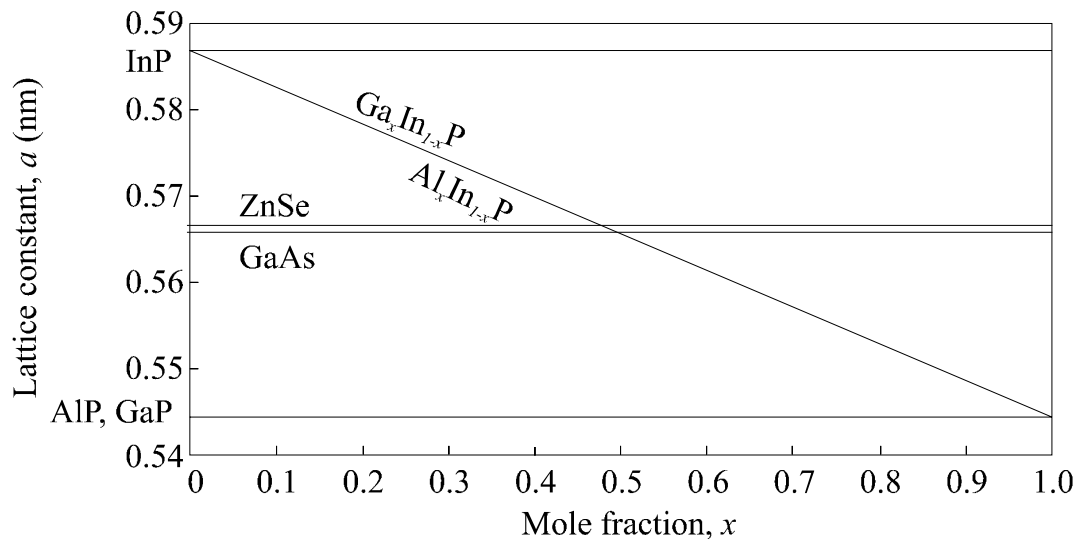


Figure 3.4: Lattice constant as a function of composition (reproduced from ref. 11).

As seen in the figure, the ternary alloys InGaP and InAlP both have a vs. x lines that pass through those of both GaAs and ZnSe, showing that these alloys can be lattice-matched to GaAs and to ZnSe. By linearly grading this III-V buffer layer from the lattice constant of GaAs to that of ZnSe, the lattice mismatch between the III-V buffer layer and II-VI layer can be minimized. The effect of a linearly-graded InGaP buffer layer is the

formation of a misfit dislocation network that is uniformly distributed in the buffer layer. Due to this effect, dislocations are more spread out than in step-graded buffer layers, resulting in a larger degree of relaxation [29].

The alloy constant, x , of a III-V ternary layer is determined by the effusion cell temperatures and the hydride flow rates. A linearly-graded alloy composition can be obtained by stepwise linearly grading one of the effusion cell temperatures over the same time period as in the case of InGaP or InAlP.

The flux from an effusion cell can be determined experimentally by using reflection high energy electron diffraction (RHEED) oscillations. For GSMBE growth of III-V materials, the temperature, and hence the flux, of the group III element is critical. Initially, the growth rate versus the temperature of the group III element is determined. The material's growth rate is simply related to the alloy fractions. The relevant equations for InGaP are:

$$\tau^{-1}_{\text{InGa}} - \tau^{-1}_{\text{Ga}} = \tau^{-1}_{\text{In}}$$

$$\% \text{In} = \tau^{-1}_{\text{In}} / \tau^{-1}_{\text{InGa}} \quad \text{where } \tau^{-1} \text{ is the rate of deposition in } \mu\text{m/hr.}$$

Below are RHEED oscillations for the growth of GaAs and then for InGaP. Since the growth rate is limited by the group III elements, the deposition rate of Ga and (In,Ga) can be obtained from RHEED oscillations during the growth of GaAs and InGaP, respectively. At the onset of growth, one oscillation occurs for every deposited monolayer. The growth rate is therefore calculated using the period of the oscillations, the lattice constant, and the time over which the oscillations are recorded.

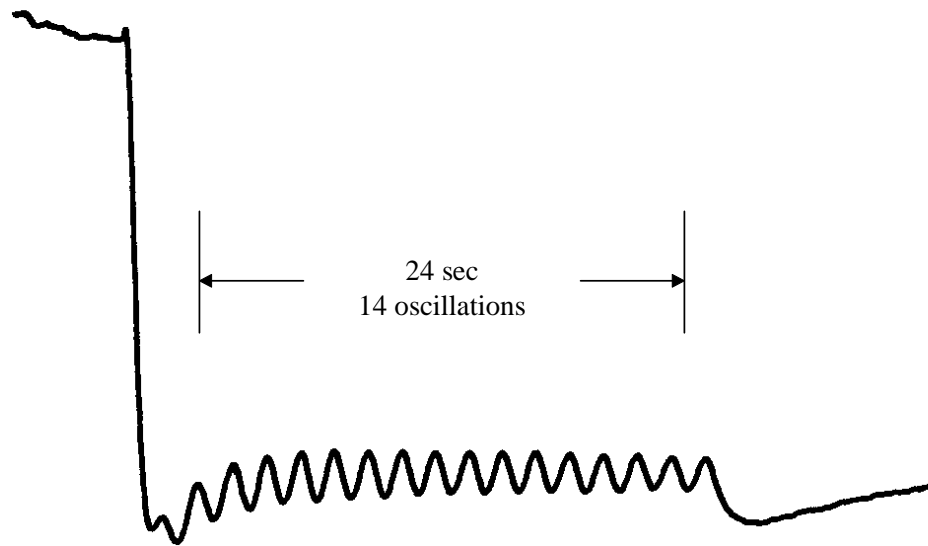


Figure 3.5a: RHEED oscillations during growth of GaAs. $\tau_{\text{Ga}}^{-1} = 0.596 \mu\text{m/hr}$.

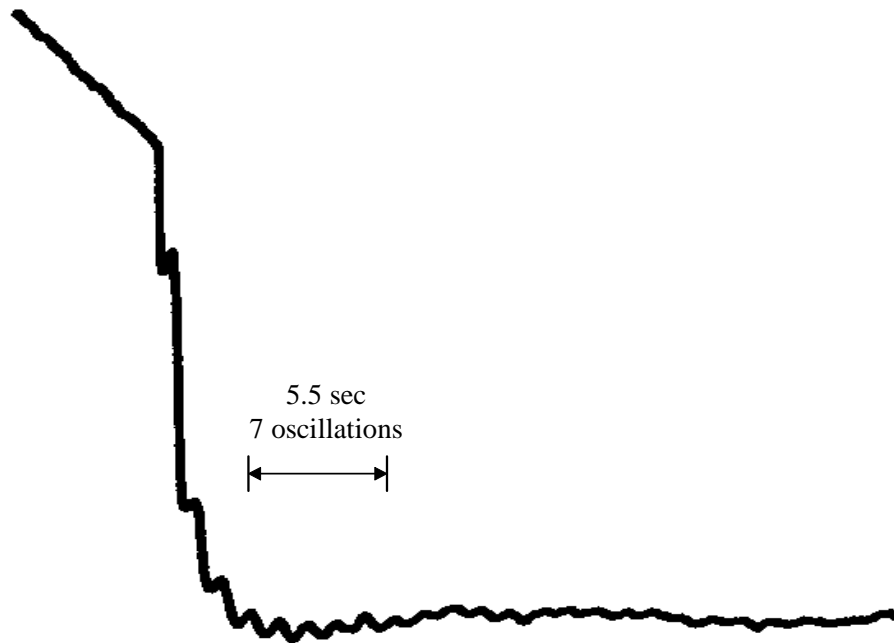


Figure 3.5b: RHEED oscillations during growth of InGaP. $\tau_{\text{InGa}}^{-1} = 1.113 \mu\text{m/hr}$.
 From these plots, $\tau_{\text{InGa}}^{-1} - \tau_{\text{Ga}}^{-1} = 1.113 - 0.596 = 0.517 \mu\text{m/hr} = \tau_{\text{In}}^{-1}$

$$\rightarrow \% \text{In} = 0.517 / 1.113 = 46\%$$

InGaP lattice-matched to GaAs requires the indium mole fraction to be 0.49 and to be lattice-matched to ZnSe, the indium mole fraction must be 0.52. Thus, this sample had a lattice constant smaller than that of GaAs.

Lattice Constant: Analysis

The degree of lattice match between ZnSe and the underlying III-V buffer layer can be determined by x-ray double crystal diffraction (XRDCD, see appendix). When ZnSe is grown on a relaxed III-V buffer layer, it may be affected by strain in two directions. d_{\perp} is the spacing between the lattice planes in the direction perpendicular to the layer surface and d_{\parallel} is the lattice spacing within the planes. The degree of lattice-match, though, can be determined from the (400) XRDCD scan.

Figure 3.6a shows the x-ray rocking curve from a sample of ZnSe grown directly on a GaAs buffer layer. The peak on the left is due to diffraction off the ZnSe layer. The sharper, higher, peak towards the center is due to diffraction off the GaAs layer. The 350 sec separation between the peaks represents a lattice-mismatch of 0.27%, since both layers were grown to be fully relaxed.

Figure 3.6b shows the x-ray rocking curve from a sample of ZnSe grown on a graded III-V InGaP buffer layer. Diffraction from the InGaP layer begins at about -3500 sec, where the InGaP is nearly lattice-matched to the GaAs, which has a peak at -3200 sec. The InGaP is graded to -3750 sec, where it is nearly lattice-matched to ZnSe. The degree of lattice-match is approximated by the relative position of the InGaP diffraction.

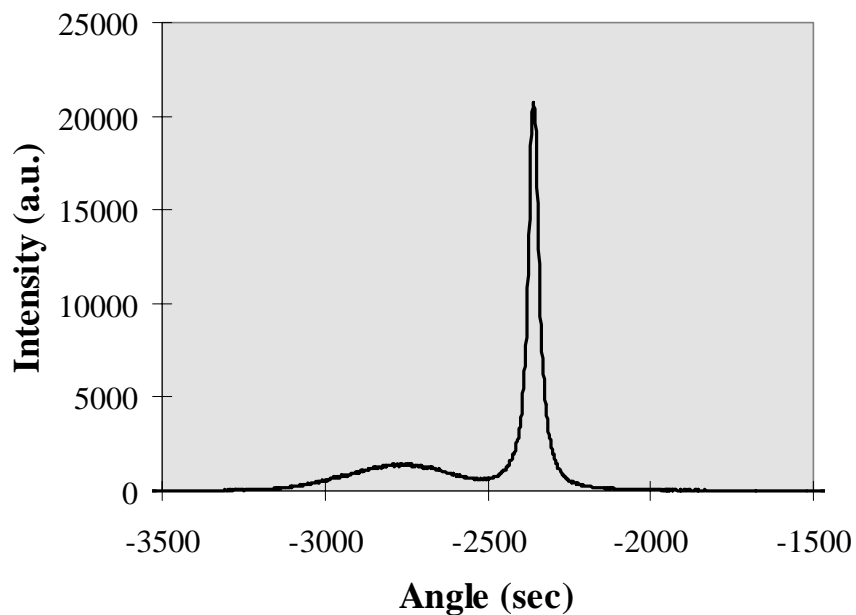


Figure 3.6a: X-Ray double crystal rocking curve of $1\mu\text{m}$ ZnSe grown on a GaAs buffer layer. ZnSe peak at -2750 sec, GaAs peak at -2400 sec. $\text{FWHM}_{\text{GaAs}} = 37$ sec.

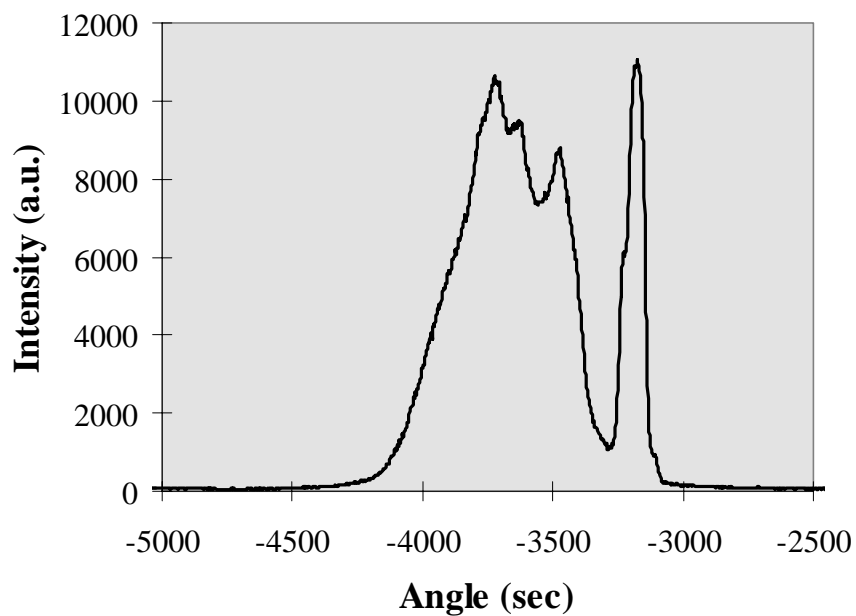


Figure 3.6b: X-Ray double crystal rocking curve of $1\mu\text{m}$ ZnSe grown on a graded InGaP buffer layer. ZnSe peak at -4000 sec, GaAs peak at -3200 sec. $\text{FWHM}_{\text{GaAs}} = 90$ sec.

Energy Gap

A large amount of research on ZnSe LEDs has been done on ZnSe grown on GaAs substrates. However, the large valence band discontinuity results in the generation of an energy spike at the heterointerface. This spike acts as a barrier for hole conduction, and a voltage drop occurs.

It is possible to change the bandgap of a ternary or a quaternary semiconductor by changing the alloy's composition. Equations relating energy gap to composition at 300K have been calculated and can be found in several sources [30]. The equations for the direct energy gap (eV) of $In_{1-x}Ga_xP$ and for $In_{1-x}Al_xP$ are given below.

$$In_{1-x}Ga_xP \quad 1.351 + 0.643x + 0.786x^2$$

$$In_{1-x}Al_xP \quad 1.351 + 2.23x$$

To provide both lattice match and a small valence band discontinuity to ZnSe, another degree of freedom is needed. These requirements have led to the research in the (In,Ga,Al)P material system as a buffer layer, as shown in figure 3.7.

To find a composition of (In,Ga,Al)P that is lattice-matched to GaAs, a region is formed by lines joining GaP, AlP, and InP. Any point directly vertical to GaAs will have the same lattice-constant as GaAs. Then, to obtain an energy gap between that of InGaP and that of InAlP, the ratio of the In, Ga, and Al concentrations are varied, while maintaining the GaAs lattice constant. In this case, an increase in the aluminum concentration increases the energy gap of the system. The precise ratio is calculated by mathematical equations which have been determined for a broad range of compounds.

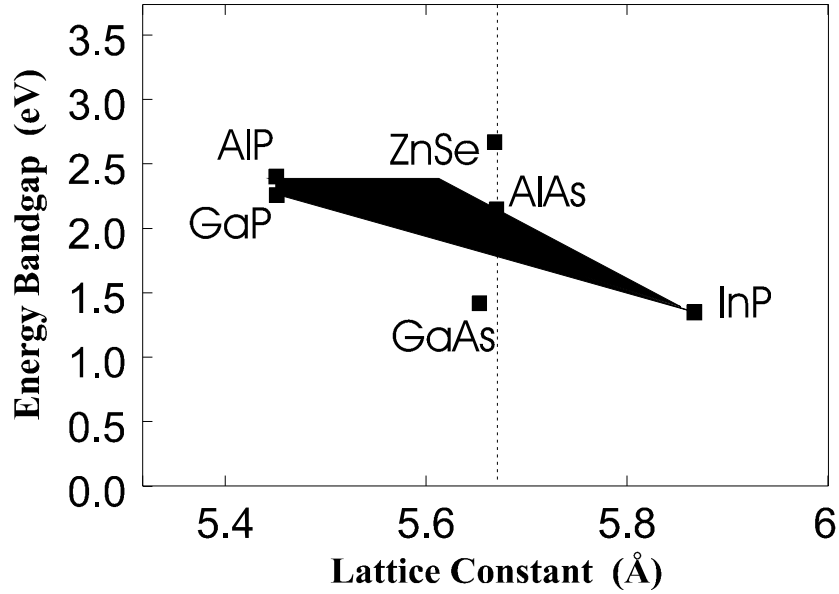


Figure 3.7: Energy bandgap (eV) versus lattice constant (a) for the (In,Ga,Al)P III-V material group and for GaAs and ZnSe.

Thus, the reason for research into the use of InGaAlP as a buffer layer is to obtain lattice-matching at both the GaAs and ZnSe interfaces as well as to minimize the valence band offset at these interfaces.

3.3 Nucleation

High quality growth of a semiconductor material by GSMBE or MBE requires a high degree of precision. Small deviations in effusion cell temperatures or fluxes result in drastic changes in the material's surface morphology. Too much or too little of one element yields an ensemble of dislocations. These dislocations have been thoroughly studied and described elsewhere [31]. Those that are most prevalent in ZnSe are shown and described below.

Poor quality ZnSe growth is generally characterized by a large concentration of paired stacking faults bounded by Shockley-type partial dislocations. These dislocations

are nucleated at or near the II-VI/GaAs interface. Figure 3.8a is a schematic of such a dislocation structure; figure 3.8b shows how the dislocation appears in plan-view TEM.

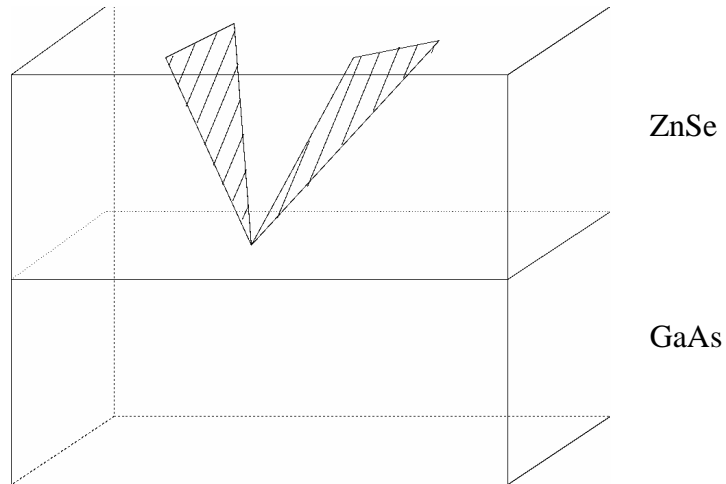


Figure 3.8a: Schematic of a pair of stacking faults surrounded by Shockley dislocations nucleated at the GaAs/ZnSe interface.

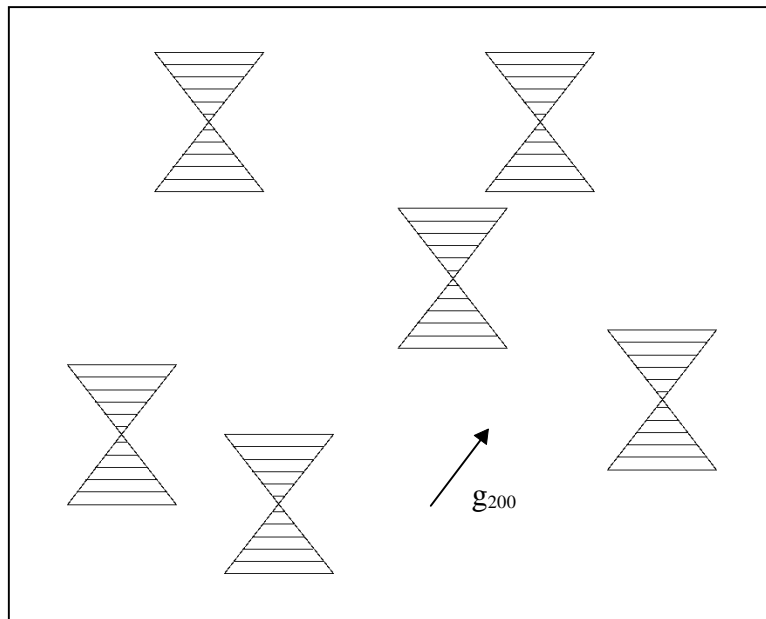


Figure 3.8b: Schematic of the plan view TEM image of a pair of stacking faults surrounded by Shockley dislocations nucleated at the GaAs/ZnSe interface.

60° misfit dislocations arise due to the 0.27% lattice-mismatch between GaAs and ZnSe. These interfacial dislocations, as discussed previously, are introduced in ZnSe

epitaxial layers in which the ZnSe thickness is larger than about 120 nm (the critical thickness of ZnSe) [32], to relax the misfit strain in the sample. Misfit dislocations appear in two forms, regular (straight) and irregular (zig-zag). It has been suggested that misfit dislocations form from dislocation half-loops which are nucleated at the film surface and glide along $\{111\}$ planes to the ZnSe/GaAs interface, where they form misfit dislocations [33]. The strain in the sample is directly related to the spacing between the 60° misfit dislocations, with large distances between misfits, suggestive of low strain. Figure 3.9 shows a plan-view TEM schematic of misfit dislocations.

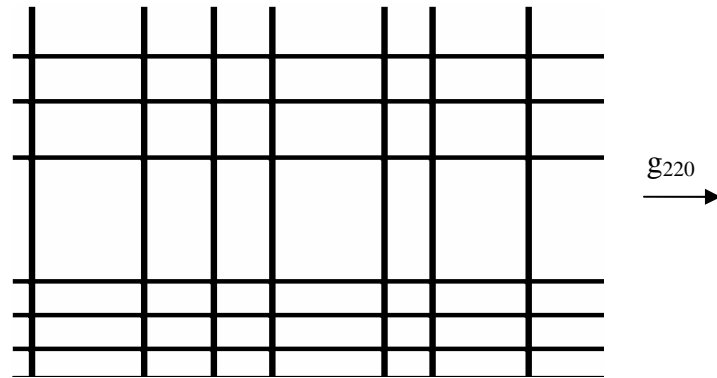


Figure 3.9: Schematic of plan-view TEM image of misfit dislocations in a ZnSe/GaAs structure.

Finally, threading dislocations are a key problem in ZnSe-based devices. Dislocations form during growth due to differences in the thermal expansion coefficients of growth materials, introduction of substitutional impurities, and simply from non-ideal stoichiometry of the interface materials [34]. The GaAs substrate inherently has about 10^3 defects cm^{-2} . Figure 3.10 schematically shows the formation of threading dislocations, in which stress has caused a column of atoms to slip out of place, resulting in the threading dislocation, or gap in the material.

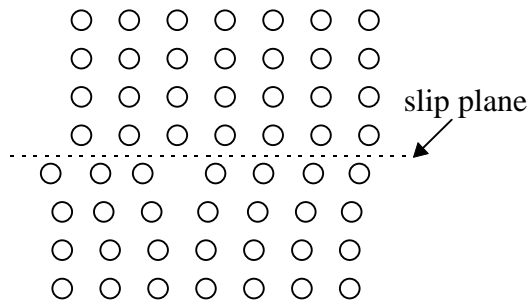


Figure 3.10: Threading dislocation formed along a slip plane (dashed line).

Chapter 4: Growth and Characterization

4.1 ZnSe/(In,Ga,Al)P/GaAs: Effect of Bandgap Match

As discussed previously, growth of ZnSe on a graded layer of (In,Ga,Al)P has the potential of providing a lattice-matched, bandgap-matched structure. This structure would inherently have few misfit dislocations in the ZnSe layer, given the lattice-matched condition. By doping the (In,Ga,Al)P p-type with beryllium, and growing a layer of p-type ZnSe:N and then a layer of n-type ZnSe:Cl, the III-V layer could potentially provide a p-type ohmic contact to the ZnSe LED, eliminating the difficulty of obtaining an ohmic contact to p-type ZnSe. Figure 4.1 shows the effect on band offset that such a scheme is assumed to have.

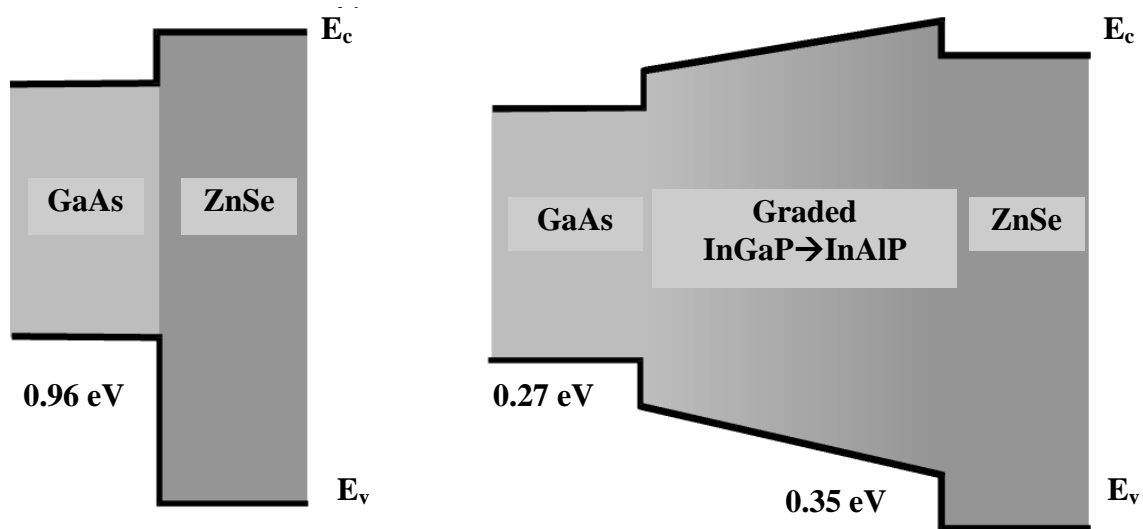


Figure 4.1: Theoretical valence band offsets for the GaAs/ZnSe structure and the GaAs/(In,Ga,Al)P/ZnSe structure. GaAs/ZnSe has a 0.96 eV valence band discontinuity; InAlP/ZnSe has a 0.35 eV valence band discontinuity.

Initial growths of ZnSe/(In,Ga,Al)P/GaAs proved that the nucleation technique used in these growths was not ideal. Photoluminescence (PL) measurements [35] (see appendix) on these samples suggested that the ZnSe epilayers were of poor quality and were highly dislocated, primarily based on the intensity of the Y_0 feature, which is suggestive of extended defects [36]. Figure 4.2 shows the photoluminescence spectra of a sample of a $1\mu\text{m}$ ZnSe epilayer grown on a layer of (In,Ga,Al)P, such that the III-V buffer layer is graded from the lattice constant of GaAs to that of ZnSe. The broad deep level luminescence band is indicative of a highly dislocated structure.

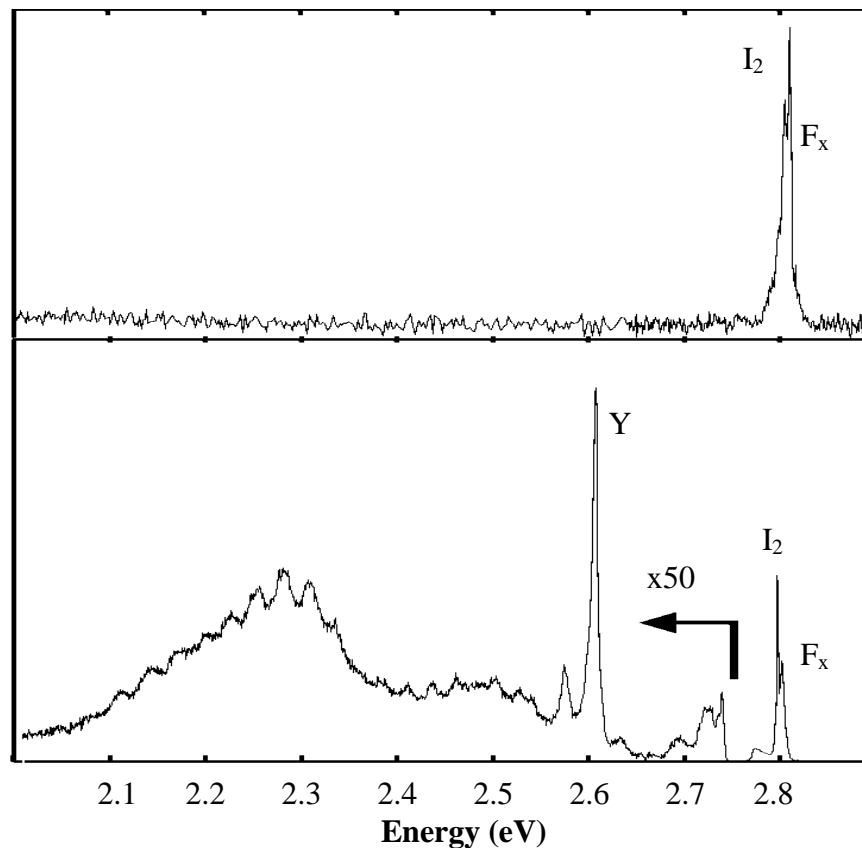


Figure 4.2: Photoluminescence scans of $1\mu\text{m}$ ZnSe grown on InAlP. The top figure shows the scan for pseudomorphic ZnSe (not relaxed). The bottom figure shows the scan for relaxed ZnSe with a deep level centered around 2.3 eV.

To verify and further analyze the InAlP/ZnSe structure, cathodoluminescence (CL) imaging was also performed (see appendix). This non-destructive technique allows the user to obtain a spatial map of the radiative and non-radiative recombination in a sample. The regions of radiative recombination appear bright; the regions of non-radiative recombination appear dark. Thus, threading dislocations appear as dark spots. Individual defects cannot be seen due primarily to the high diffusion constant of the electrons, and due to the sample being at room temperature.

CL scans were obtained for a group of five samples, each of which had the same basic structure of 1 μ m MBE-ZnSe epilayers grown on 4 μ m relaxed GSMBE-(In,Ga,Al)P buffer layers on GaAs. In each case, the growth of ZnSe was initiated by simultaneously opening both the zinc and the selenium shutters. Table 4.1 shows the III-V buffer layers used for the samples and the lattice constants associated with each. The notation, $a_{\text{GaAs}} \rightarrow a_{\text{ZnSe}}$, refers to a layer of (In,Ga)P with an in-plane lattice constant graded from that of GaAs to that of ZnSe.

Sample #	(In,Ga,Al)P Buffer	Lattice constant, a
1	(In,Ga)P	$a = a_{\text{GaAs}}$
2	(In,Ga)P	$a = a_{\text{GaAs}} \rightarrow a_{\text{ZnSe}}$
3	(In,Al)P	$a = a_{\text{GaAs}}$
4	(In,Al)P	$a = a_{\text{GaAs}} \rightarrow a_{\text{ZnSe}}$
5	(In,Ga,Al)P	$a = a_{\text{GaAs}} \rightarrow a_{\text{ZnSe}}$

Table 4.1: (In,Ga,Al)P layers used as buffers for 1 μ m ZnSe epilayers.

The CL images in figure 4.3 show the similarity between the radiative recombination in each of the described samples. The first image is of sample 2 (figure 4.3a), which has a III-V (In,Ga)P buffer layer that is graded from the lattice constant of GaAs to that of ZnSe. Such a structure should have a low density of misfit dislocations in the ZnSe. The image of sample 3 (figure 4.3b), which has an (In,Al)P layer with the lattice constant of GaAs, shows a very similar recombination structure to that of sample 2, even though this sample contains a 0.27% lattice-mismatch and includes aluminum at the III-V/II-VI heterointerface. Finally, sample 5 (figure 4.3c) is a lattice-matched (In,Ga,Al)P structure. The images of samples 3 and 5 look nearly identical, showing the small role that lattice match plays in the defect density of these samples, since sample 3 is lattice-mismatched and sample 5 is lattice-matched.

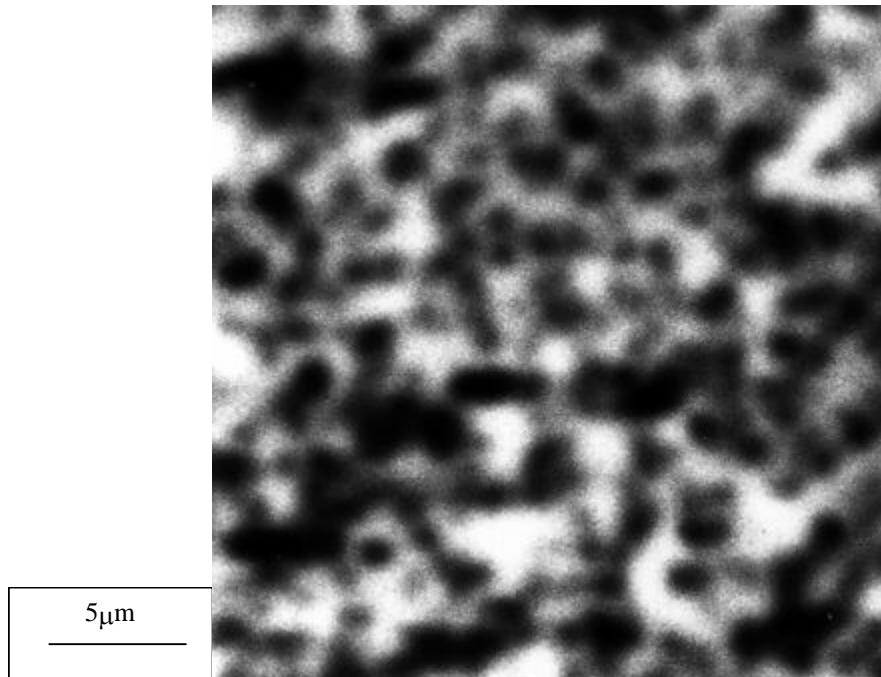


Figure 4.3a: CL of Sample #2--1μm ZnSe on 4μm relaxed graded layer of (In,Ga)P.
T = 300K; Mag = 1700x.

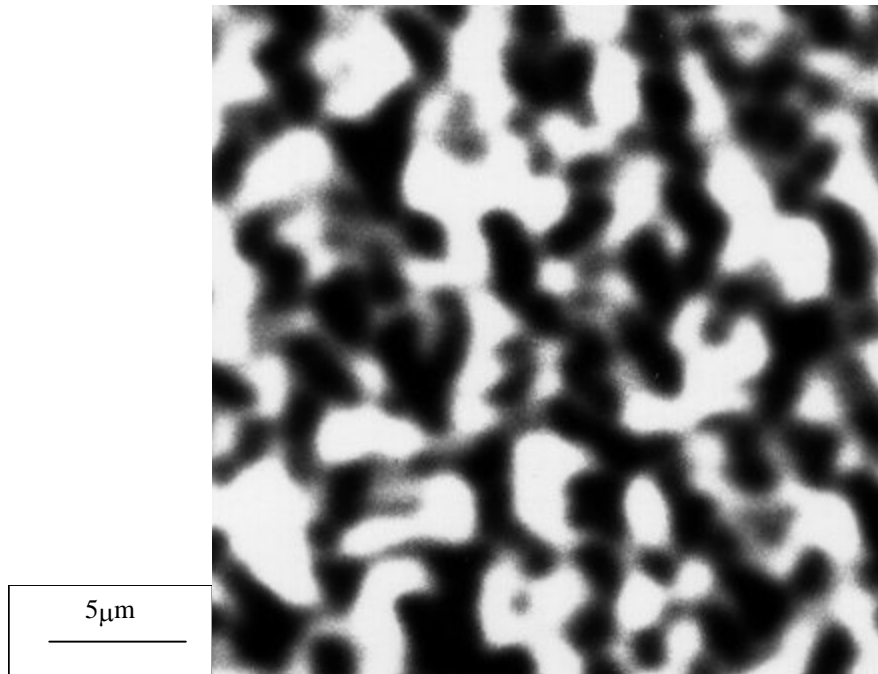


Figure 4.3b: CL of Sample #3--1 μ m ZnSe on 4 μ m relaxed stepped layer of (In,Al)P.
T = 300K; Mag = 1700x.

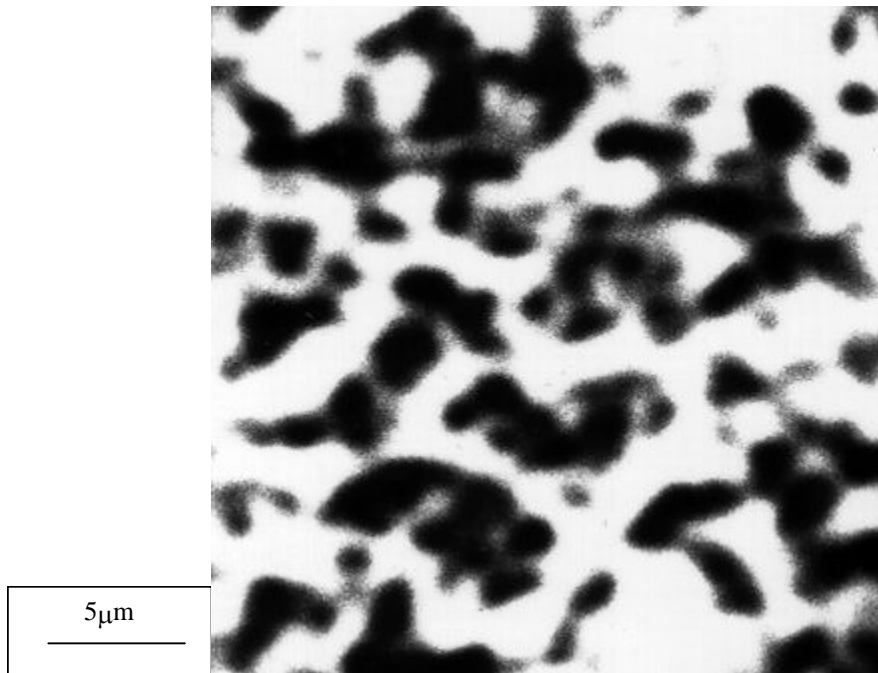


Figure 4.3c: CL of Sample #5--1 μ m ZnSe on 4 μ m relaxed graded layer of (In,Ga,Al)P.
T = 300K; Mag = 1700x.

To determine the actual defect density for these structures, etch pit density measurements were performed (see appendix). The defect density in each of these samples was greater than 10^7 cm^{-2} . Thus, initial CL characterization of ZnSe on lattice-matched (In,Ga,Al)P surfaces indicated the presence of an unexpectedly high density of dislocations. The origin of such a high density of defects was speculated to be due to the surface chemistry and to the ZnSe nucleation conditions.

An atomic force micrograph is shown in figure 4.4 for sample 5 (see appendix).

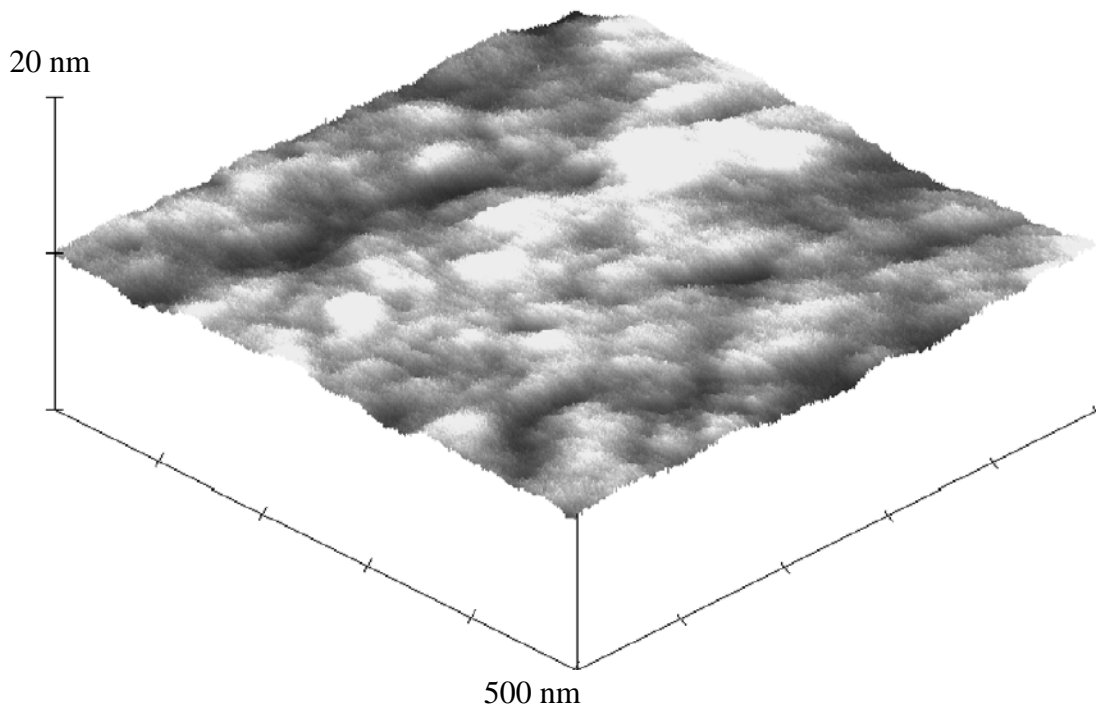


Figure 4.4: Atomic force micrograph of $1\mu\text{m}$ ZnSe film grown by MBE on $4\mu\text{m}$ linearly graded (In,Ga,Al)P buffer layer. The mean roughness value over a $500 \text{ nm} \times 500 \text{ nm}$ area was 4\AA .

Though the corresponding CL image of sample 5 shows a large percentage of non-radiative recombination, the AFM results are indicative of a very smooth growth front based on the low R_a value (the mean value of the height of the sample's surface) of 4\AA .

The lack of correlation between the defect density and the strain in the samples, however, suggests that the problem with these growths is primarily due to the details of the nucleation. Several ZnSe/GaAs nucleation studies have been recently reported [37].

4.2 ZnSe/GaAs: Effect of Nucleation

A nucleation study is complicated by the many factors involved. At a particular interface, each material can be rich in any one of its constituent elements. Growth of the overlying layer can begin after an exposure to any one of its elements. Thus, the (In,Ga,Al)P/ZnSe heterointerface has numerous nucleation possibilities. To simplify the situation, the ZnSe/GaAs nucleation process can be studied first, to determine the ideal growth parameters in terms of the defect density of the overlying ZnSe. Then this structure, using a very thin layer of GaAs, can be grown on a graded (In,Ga,Al)P buffer layer. In this way, the lattice-match afforded by an (In,Ga,Al)P buffer layer can be used, while taking advantage of the previously studied ZnSe/GaAs nucleation. A very thin, pseudomorphic layer of GaAs will be strained to maintain the lattice constant of the underlying (In,Ga,Al)P.

GaAs

GaAs can be terminated such that it is either Ga-rich or As-rich, and the percentage in each case may be intentionally varied. These different terminations create different GaAs surface reconstructions, which can be monitored by RHEED (see appendix).

All of the GaAs was grown at a substrate temperature of 600°C, as determined by an optical pyrometer. After the growth of the buffer layer at 600°C, the surface exhibited an As-stabilized (2x4) reconstruction. As the substrate temperature decreased to 530°C with the sample exposed to an As flux, the (2x4) surface reconstruction changed to a c(4x4) reconstruction. This reconstruction remained stable even after the arsine flow into the chamber was terminated at 350°C. To prepare a buffer layer exhibiting a (2x4) reconstruction at room temperature, the substrate temperature and the As flux were simultaneously lowered after growth. The arsine flow was reduced to 0.1 sccm, which was sufficient to maintain the (2x4) reconstruction. The RHEED pattern was closely monitored during this process, as seen by the similarity of the post-growth (2x4) RHEED patterns at a high and a low temperature in figure 4.5.



Figure 4.5a: RHEED pattern of (2x4)-reconstructed GaAs at growth temperature ($T_c=640^\circ\text{C}$).



Figure 4.5b: RHEED pattern of (2x4)-reconstructed GaAs before transfer ($T_c=270^\circ\text{C}$).

The c(4x4) reconstruction is characterized by 100% As surface coverage; the (2x4) surface has 75% As coverage [38]. Schematics are shown in figure 4.6.

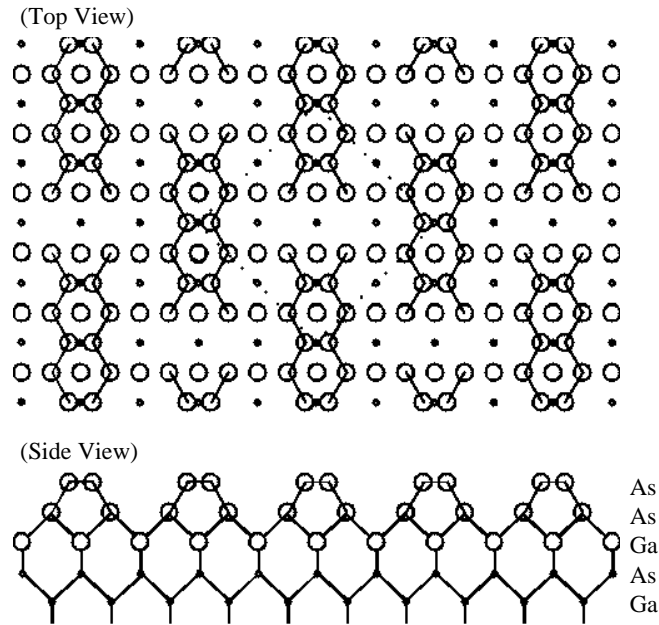


Figure 4.6a: Top view and side view of c(4x4)-reconstructed GaAs (100% arsine surface coverage). (reproduced from ref. 38)

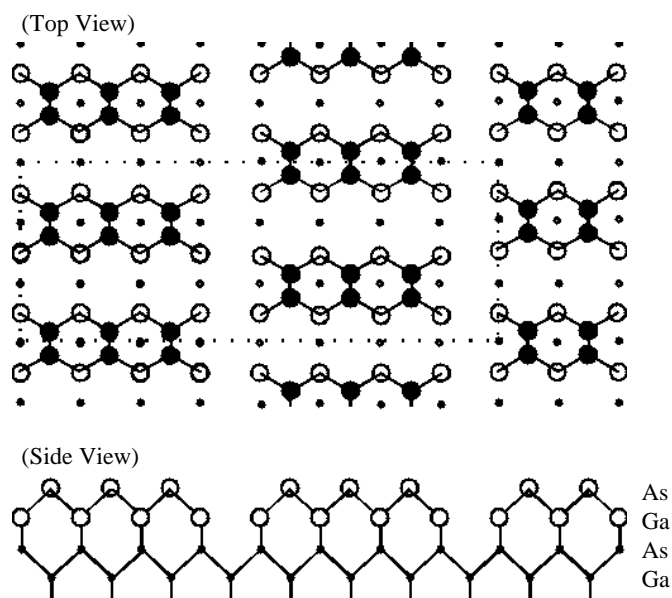


Figure 4.6b: Top view and side view of (2x4)-reconstructed GaAs (75% arsine surface coverage). (reproduced from ref. 38)

ZnSe

ZnSe can be grown in several ways on the GaAs underlayer. Growth may include a pre-exposure of either Zn or Se, for varying periods of time. Another technique that has been studied over the past few years for ZnSe growth is Migration-Enhanced Epitaxy (MEE) [39]. MEE involves alternately chopping the beams produced from the effusion cells in a cyclic fashion. One cycle of MEE represents one opening of each shutter. Many variables are involved in MEE—each shutter must be opened long enough to fill all surface sites (to allow a full monolayer of the element to form on the surface) and enough time must be allowed in the interim between shutter openings to ensure that the previously deposited atom finds an energetically favorable site to incorporate into the lattice. MEE increases the atom mobility on the surface by allowing time for surface diffusion prior to incorporating. This technique has been investigated in this study.

ZnSe/GaAs

The surface stoichiometry for the growth of ZnSe on GaAs can be varied in many ways, as discussed above. One way to vary the surface chemistry is to change the surface reconstruction pattern of the III-V buffer layer. Another means of varying the surface chemistry is to start the ZnSe growth with a pre-exposure of zinc or selenium atoms.

Figure 4.7 shows several possible surface configurations, each corresponding to a different valence band offset between the ZnSe and the GaAs, with the GaAs having a higher valence band energy, hindering hole injection into the II-VI layer in a ZnSe-based LED structure. The trend in the band offsets, based on theoretical analysis, is related to the establishment of neutral interfaces with different atomic configurations [40].

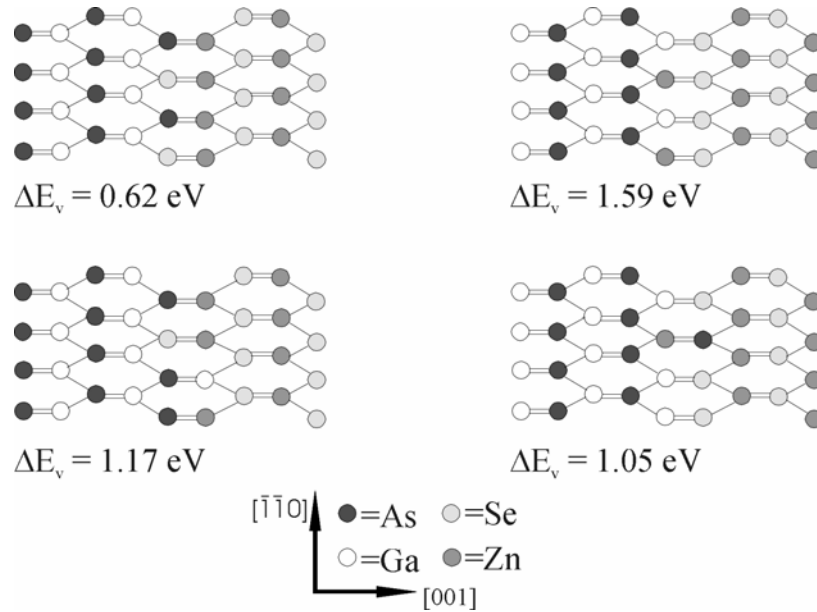


Figure 4.7: Surface configurations for ZnSe on GaAs. The trend in band offsets is based on theoretical analysis.

The top two configurations can result from 1:1 compositions of gallium to arsine and zinc to selenium at the interface. The lower left configuration shows an arsine-rich GaAs surface and a zinc-rich ZnSe growth start. The lower right configuration shows a gallium-rich GaAs surface and a selenium-rich ZnSe growth start.

Thus the variety of possible nucleation processes is evident, even for the seemingly simple growth of ZnSe on GaAs.

MBE-ZnSe/c(4x4)-reconstructed GaAs

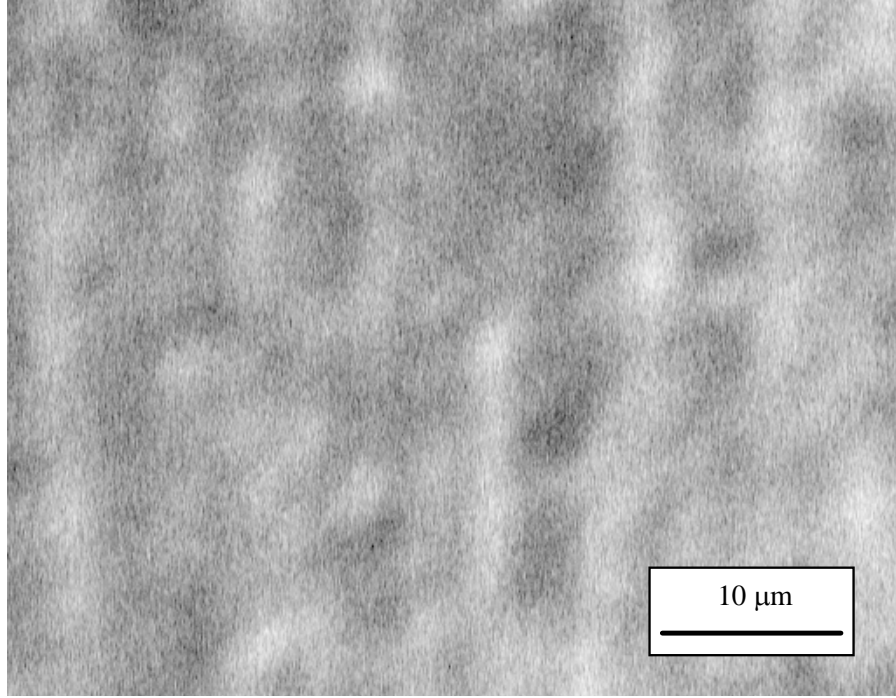
The first set of growths involved ZnSe grown on c(4x4)-reconstructed GaAs, with and without pre-exposures of Zn and Se. The table below details the growths.

Sample #	GaAs Buffer?	Pre-Exposure?	Pre-Exp Time
6	Yes	Se	1 min
7	Yes	Zn	2 mins
8	Yes	No	

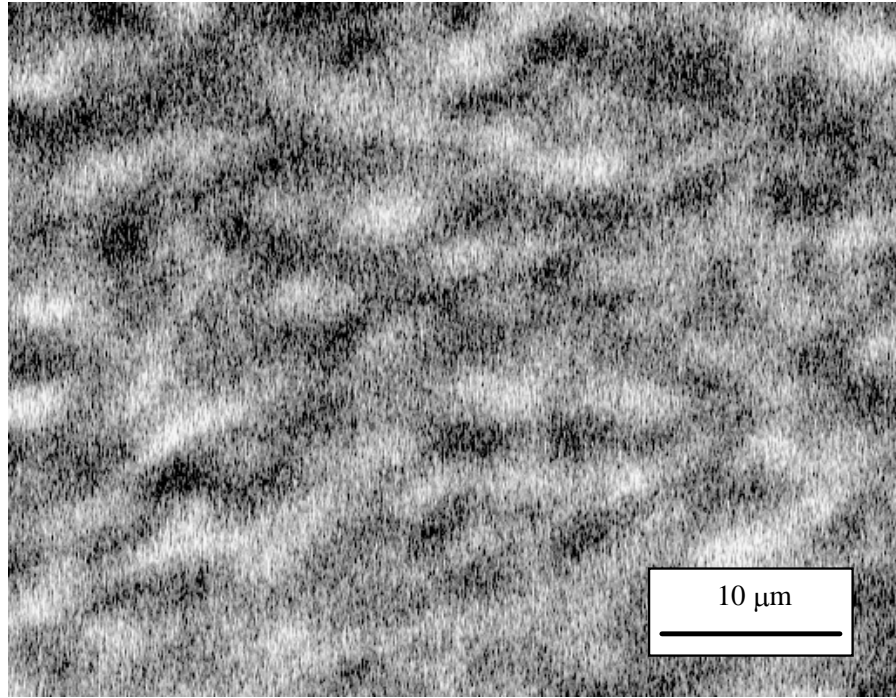
Table 4.2: Pre-exposures used in MBE-ZnSe/c(4x4)-reconstructed GaAs growths

These growths were intended to primarily give information about the effect of the various nucleation techniques on the defect densities in the overlying ZnSe. Therefore, the growths were primarily characterized by CL and EPD. Figure 4.8 shows the CL images for each sample. Each has an estimated defect density of over 10^7 cm⁻², as determined both by CL and by etch pit measurements.

(a)



(b)



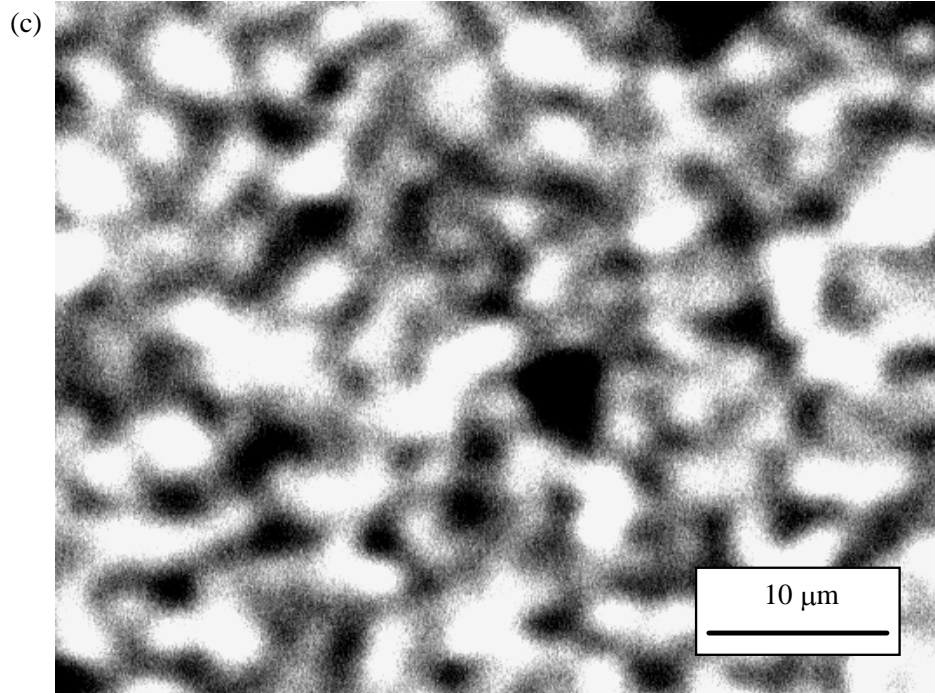


Figure 4.8: (a) MBE-ZnSe/c(4x4)-reconstructed GaAs with Zn and Se shutters opened simultaneously; (b) MBE-ZnSe/c(4x4)-reconstructed GaAs with a 2 minute Zn pre-exposure; (c) MBE-ZnSe/c(4x4)-reconstructed GaAs with 1 min Se pre-exposure.

Though the contrast in these three images differs, the percentage of radiative to non-radiative recombination seems nearly identical. This suggests that the c(4x4)-reconstructed GaAs surface results in a high defect density ($> 10^7 \text{ cm}^{-2}$), regardless of the pre-exposure before the MBE-ZnSe growth.

Another means of characterizing the effects of the nucleation conditions is the use of atomic force microscopy (AFM) (see appendix). Figure 4.9 shows the atomic force micrograph from a sample of ZnSe grown on c(4x4)-reconstructed GaAs with a two minute Zn pre-exposure. A mean roughness (R_a) of 9Å was measured over a 500 nm x 500 nm area.

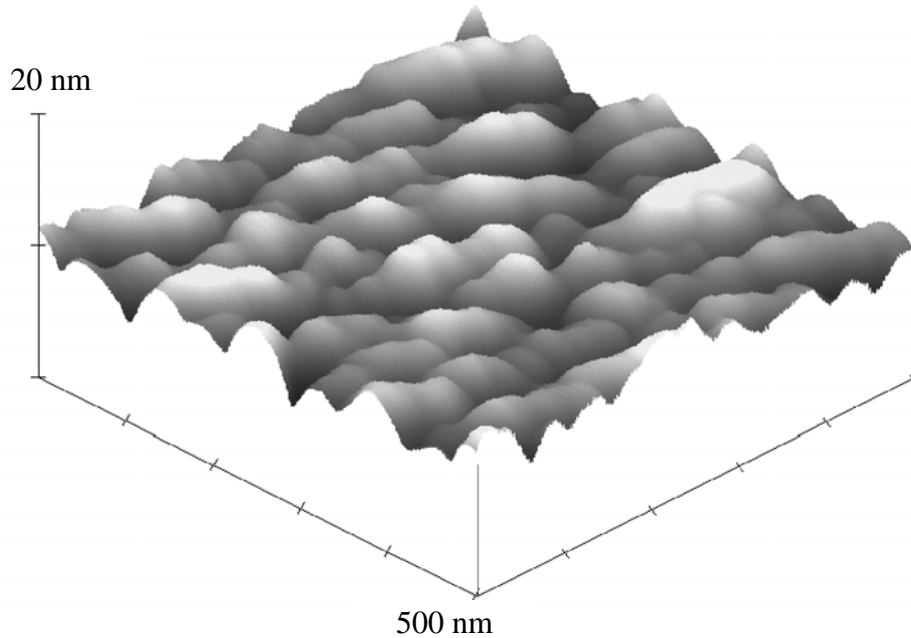


Figure 4.9: Atomic force micrograph of 1 μm ZnSe film grown by MBE on a Zn pre-exposed c(4x4)-reconstructed GaAs buffer layer (sample 7).

MBE-ZnSe/(2x4)-reconstructed GaAs

The second set of growths involved ZnSe grown on (2x4)-reconstructed GaAs, with two minute pre-exposures of Zn (sample 9). This same structure was grown twice to strengthen the validity of the results. Figure 4.10 shows the CL image obtained from this sample.

The CL image of this sample shows that the growth of ZnSe on (2x4)-reconstructed GaAs results in a much lower density of defects than for the growth on c(4x4)-reconstructed GaAs. This is clear by the decreased percentage of dark areas, which are representative of non-radiative recombination sites. The dark area in the upper left portion of the image is the result of the sample mount.

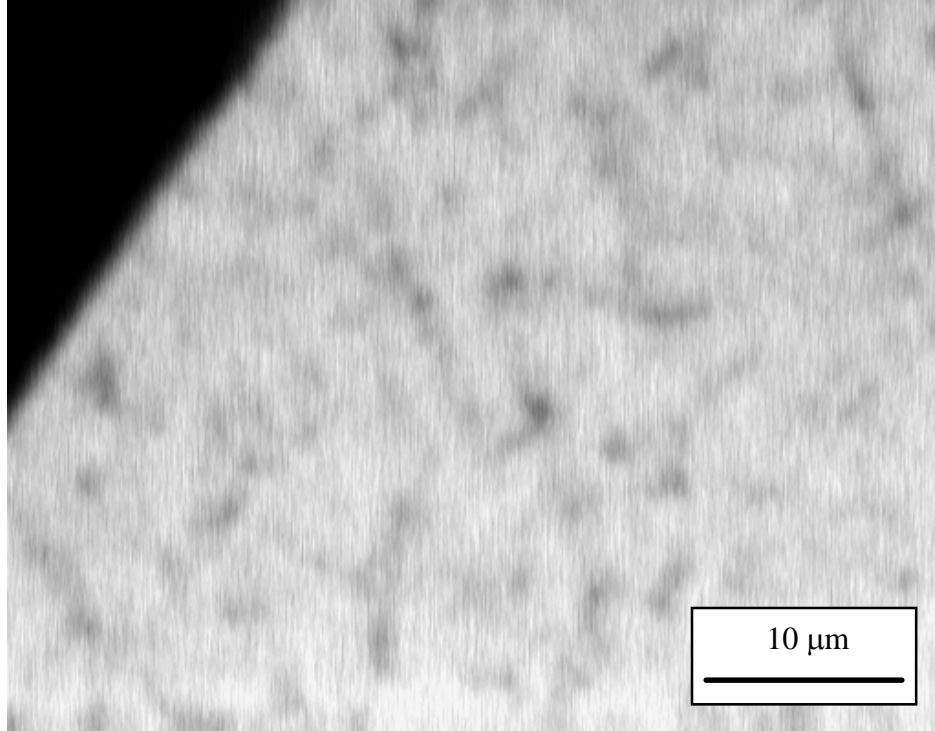


Figure 4.10: Room temperature CL image of MBE-ZnSe/(2x4)-reconstructed GaAs with a 2 min Zn pre-exposure (sample 9); Mag=1700x.

AFM was also performed on this sample and the results are shown in figure 4.11. The mean roughness (R_a) value was 7Å over a 500 nm x 500 nm area, lower than that found for ZnSe grown on a c(4x4)-reconstructed GaAs buffer layer.

In other sets of similar films, the R_a values from the ZnSe epilayer grown on c(4x4)-reconstructed GaAs were consistently larger than the values measured from the ZnSe epilayers grown on (2x4)-reconstructed GaAs.

Etch pit density (EPD) measurements of ZnSe grown on (2x4)-reconstructed GaAs reveal an EPD of less than 10^6 cm^{-2} , a factor of ten lower than that of ZnSe grown on c(4x4)-reconstructed GaAs.

Reduced defect densities in ZnSe epilayers grown on (2x4)-reconstructed GaAs agrees with another recent study [41]. The complexity of the ZnSe/GaAs interfacial layer

makes it difficult to isolate the reason for the reduced defect density in ZnSe grown on (2x4)-reconstructed GaAs surfaces compared to ZnSe grown on c(4x4)-reconstructed GaAs surfaces. A contributing factor for the difference is that a more charge neutral interface is formed on a (2x4)-reconstructed GaAs surface as opposed to a c(4x4)-reconstructed GaAs surface. A completely charge neutral interface can be formed if the anion plane is 50% As and 50% Se. (2x4)-reconstructed GaAs has, on average, a 75% As surface coverage, which is lower than the 100% surface coverage of c(4x4)-reconstructed GaAs [42].

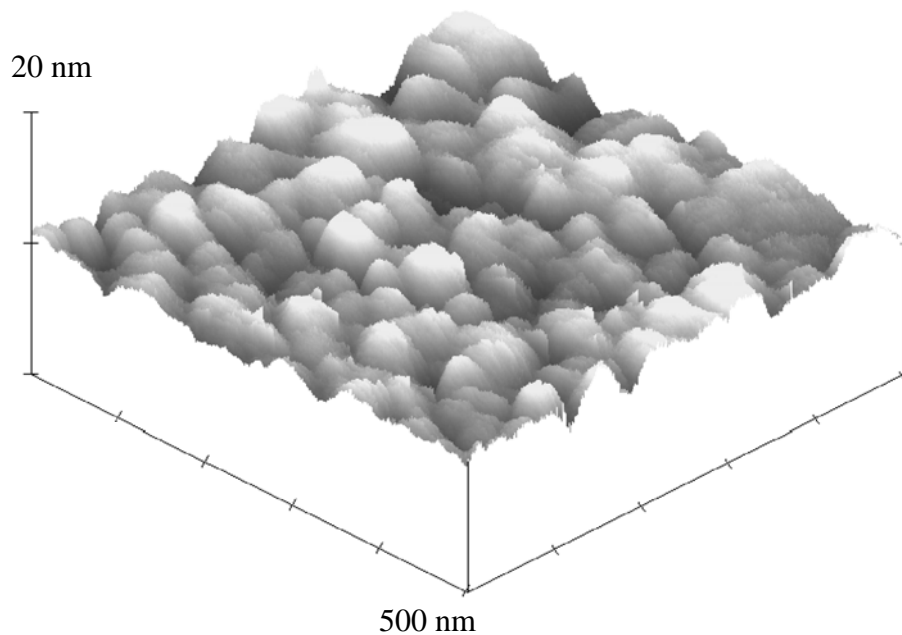


Figure 4.11: Atomic force micrograph of 1 μm ZnSe film grown by MBE on a Zn pre-exposed (2x4)-reconstructed GaAs buffer layer (sample 9).

Migration Enhanced Epitaxy

Characterization of the set of MEE-initiated samples did not demonstrate a noticeable difference in defect densities between the MBE and the MEE growth of ZnSe

on GaAs exhibiting a (2x4) reconstruction. The MEE growth was performed at 260°C, following a one minute Zn pre-exposure. Each cycle consisted of 3 seconds of Se, a 2 second delay, and 3 seconds Zn. Ten cycles were performed at the initial low temperature, and then 24 more cycles were performed as the substrate was ramped to the growth temperature of 300°C. The corresponding CL images are shown in figure 4.12.

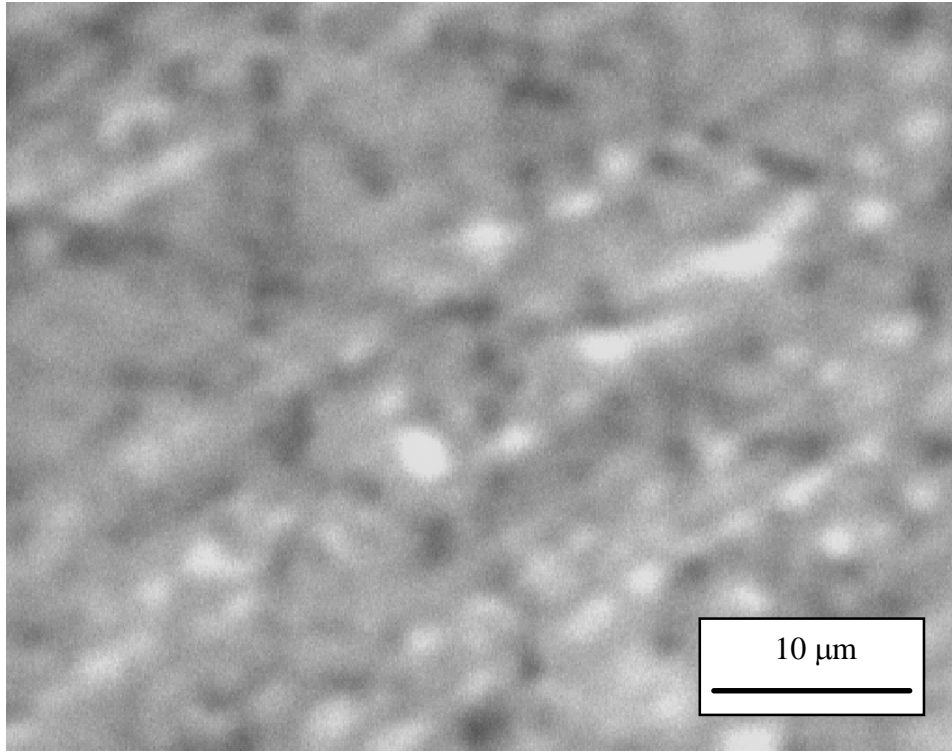


Figure 4.12a: 1 μ m ZnSe grown on c(4x4)-reconstructed GaAs with a one minute Zn pre-exposure followed by ten cycles of MEE (cycle = 3 sec Se, 2 sec delay, 3 sec Zn) at 260°C and 24 more cycles of MEE while ramping to the growth temperature.

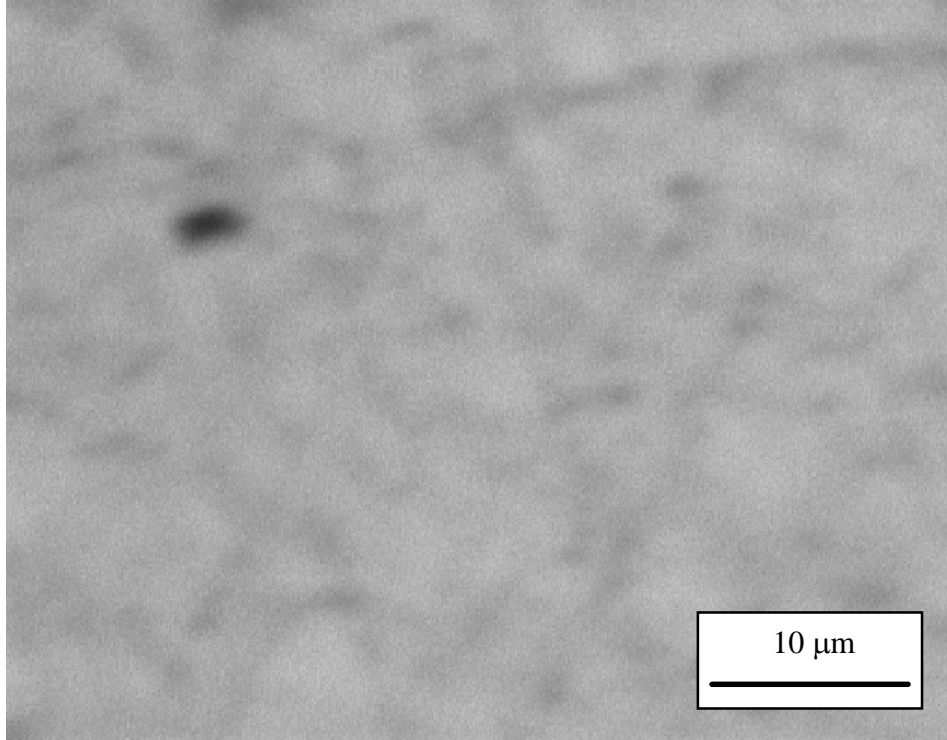


Figure 4.12b: 1 μm ZnSe grown on (2x4)-reconstructed GaAs with a one minute Zn pre-exposure followed by ten cycles of MEE (cycle = 3 sec Se, 2 sec delay, 3 sec Zn) at 260°C and 24 more cycles of MEE while ramping to the growth temperature.

The CL images shown above do not demonstrate a noticeable difference between growth of ZnSe with an MEE initiation on c(4x4)-reconstructed GaAs and growth on (2x4)-reconstructed GaAs. In addition, the CL images of ZnSe grown directly on (2x4)-reconstructed GaAs show a lower defect density than that of ZnSe grown on (2x4)-reconstructed GaAs with an MEE growth initiation. This suggests that it is not advantageous to employ the MEE growth technique.

4.3 ZnSe/GaAs/(In,Ga)P: Effect of Lattice Mismatch

Once the growth of ZnSe on GaAs had been significantly improved by pre-exposing a (2x4)-reconstructed GaAs to Zn before MBE-ZnSe growth, the effect of

lattice mismatch on defect density could be studied. A pseudomorphic layer of GaAs will grow on a relaxed (In,Ga)P graded buffer layer without altering the lattice constant of the topmost monolayers of (In,Ga)P. Such a pseudomorphic layer of GaAs assumes the lattice constant of the underlying layers.

Samples in this study utilized buffer layers constructed from 4 μm relaxed graded layers of (In,Ga)P, with a pseudomorphic eight monolayer GaAs cap. The (In,Ga)P was graded from the lattice constant of GaAs to that of ZnSe. Thus, the final monolayers of (In,Ga)P had a lattice constant close to that of ZnSe. The degree of lattice match was analyzed by X-Ray Double Crystal Diffraction. The pseudomorphic layer of GaAs grown on the (In,Ga)P was necessarily under tensile strain, since the relaxed lattice constant of GaAs is 0.27% smaller than that of ZnSe.

In order to compare these samples to those used in the nucleation study, two growths were performed. The sample structures are shown schematically in figure 4.13.

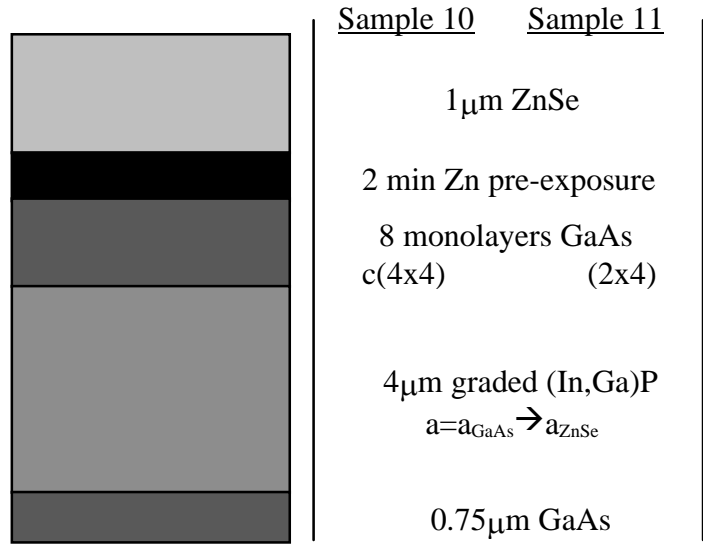


Figure 4.13: Schematic of growths used to study the effect of lattice-mismatch.

Each structure includes a graded layer of (In,Ga)P such that there is no lattice-mismatch at the III-V/II-VI heterointerface. Sample 10 has a c(4x4)-reconstructed GaAs cap and sample 11 has a (2x4)-reconstructed GaAs cap.

To ensure that ZnSe growth on the GaAs cap was not impeded by the inclusion of a graded layer of (In,Ga)P, transmission electron microscopy (TEM) was used to compare the interfaces of sample 9, which simply involved the growth of MBE-ZnSe on a Zn pre-exposed (2x4)-reconstructed GaAs surface, and that of sample 11, which incorporated the graded (In,Ga)P buffer layer. To enable direct comparison, each of the TEM micrographs were taken under the 220 bragg condition. These results are shown in figure 4.14.

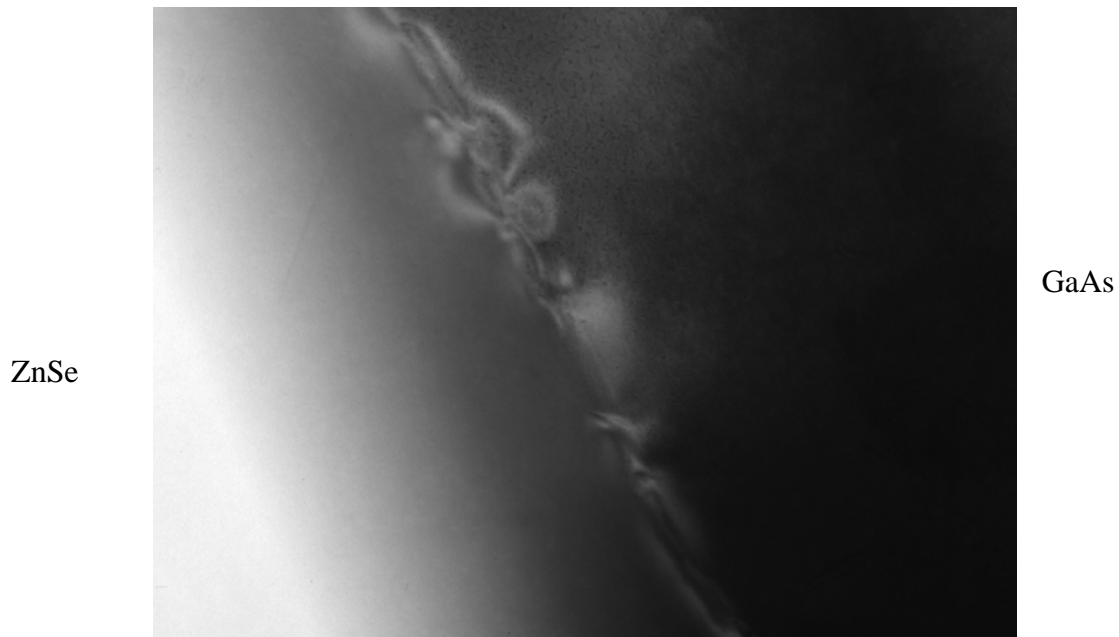


Figure 4.14a: TEM micrograph of sample 9 (1 μ m ZnSe on (2x4)-reconstructed GaAs). Micrograph is about 4 μ m wide. TEM courtesy of Jody House.

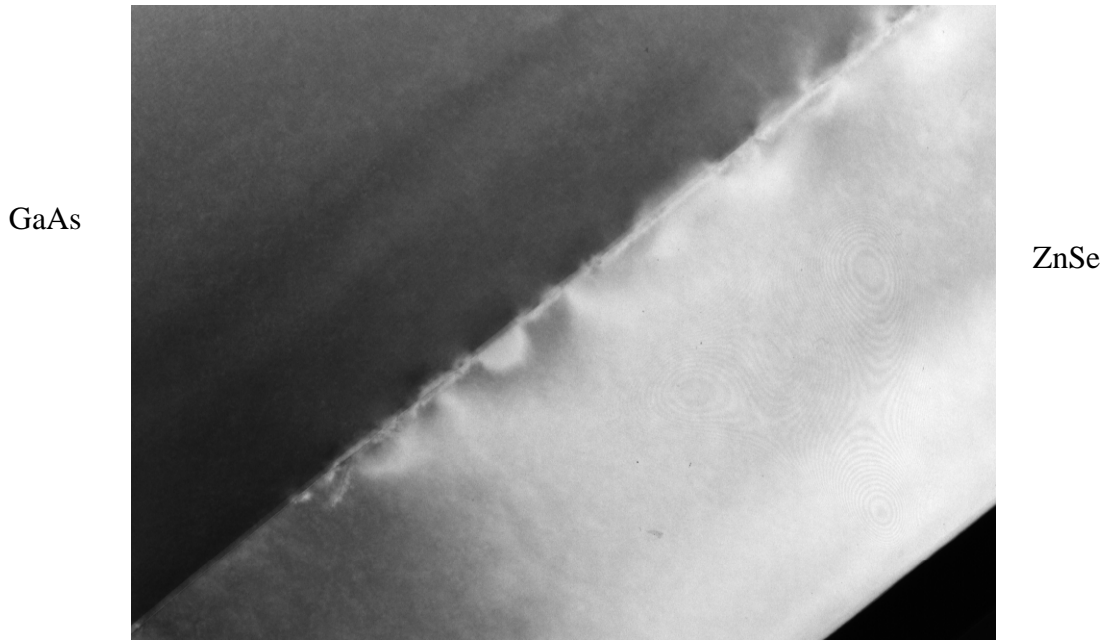


Figure 4.14b: TEM micrograph of sample 11 ($1\mu\text{m}$ ZnSe on (2x4)-reconstructed GaAs on a graded (In,Ga)P buffer layer). Micrograph is about $2.5\mu\text{m}$ wide. TEM courtesy of Jody House.

These micrographs verify that the growth of MBE-ZnSe on a pre-exposed surface of (2x4)-reconstructed GaAs was not hampered by the underlying graded (In,Ga)P buffer layer of sample 11. This conclusion is based on the similarity of the features in the two micrographs, each showing a fairly smooth growth initiation with no visible threading dislocations or stacking faults.

Given the high magnification of TEM imaging, the technique does not reveal any threading dislocations in these samples, requiring other techniques to measure defect density. Room temperature CL images are shown (figures 4.15a and 4.16a) for each sample, with their corresponding etch pit density Nomarski photographs (figures 4.15b and 4.16b). Etch pitting (see appendix) was performed with a bromine-methanol solution consisting of 1% bromine. The samples were each placed in the etchant for one second to etch 250 nm. This solution etches the area around a dislocation more rapidly than

undislocated areas. In this way, threading dislocations are exposed. EPD is a fairly reliable means of estimating the defect density of a semiconductor [43].

The dark spots seen in the CL image of figure 4.15a are due to threading dislocations, while the dark lines seen in figure 4.16a are due to misfit dislocations. The CL image of sample 10 (figure 4.15a) appears nearly identical to that of sample 7 (figure 4.8b) for which no (In,Ga)P layer was used and thus the sample had a large lattice-mismatch at the II-VI/III-V heterointerface. This suggests that the high dislocation density in these samples is due to poor nucleation and that the reduction of the lattice-mismatch does not have a noticeable effect. The density of threading dislocations is estimated to be approximately 10^7 cm^{-2} for sample 10.

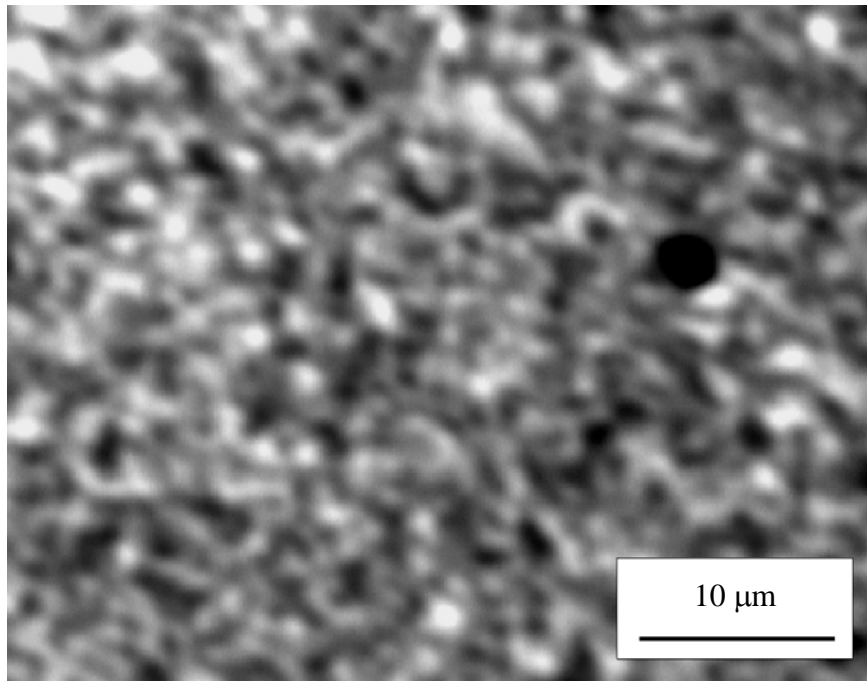


Figure 4.15a: Room temperature CL of 1 μm ZnSe film grown by MBE on 4 μm linearly graded (In,Ga)P buffer layer with a two minute Zn-exposed eight monolayer c(4x4)-reconstructed GaAs layer between the (In,Ga)P and ZnSe (sample 10). Mag = 1700x.

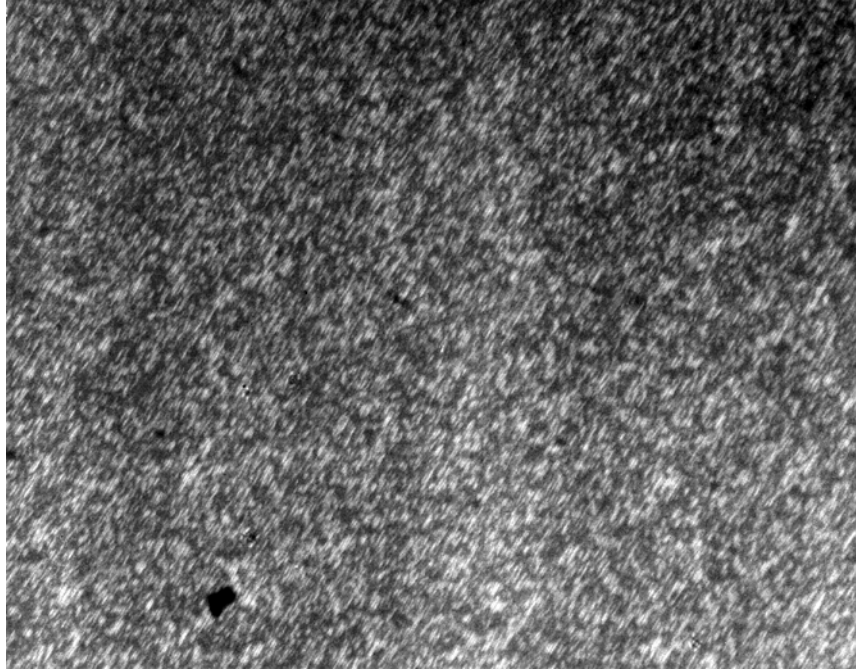


Figure 4.15b: EPD photograph of 1 μ m ZnSe film grown by MBE on 4 μ m linearly graded (In,Ga)P buffer layer with a two minute Zn-exposed eight monolayer c(4x4)-reconstructed GaAs layer between the (In,Ga)P and ZnSe (sample 10). Mag=400x. EPD=3x10⁷ cm⁻².

In contrast, the CL image of sample 11 (figure 4.16b) primarily exhibits misfit dislocations with faint features due to various types of irregularities in the crystal lattice. Since CL imaging shows enhanced contrast at misfit dislocations, these represent the dominant form of dislocations in this film. This suggests that the growth of ZnSe on (2x4)-reconstructed GaAs minimizes threading dislocations arising from the II-VI/III-V nucleation such that the slight lattice-mismatch in sample 11 plays the primary role in the dislocation process. The average spacing of the misfit lines is approximately 3 μ m, indicative of the close lattice-match [44], which is confirmed by x-ray diffraction measurements. CL and EPD measurements both suggest a threading dislocation density of 10⁶ cm⁻² in this sample. The remaining dislocations are speculated to arise either from

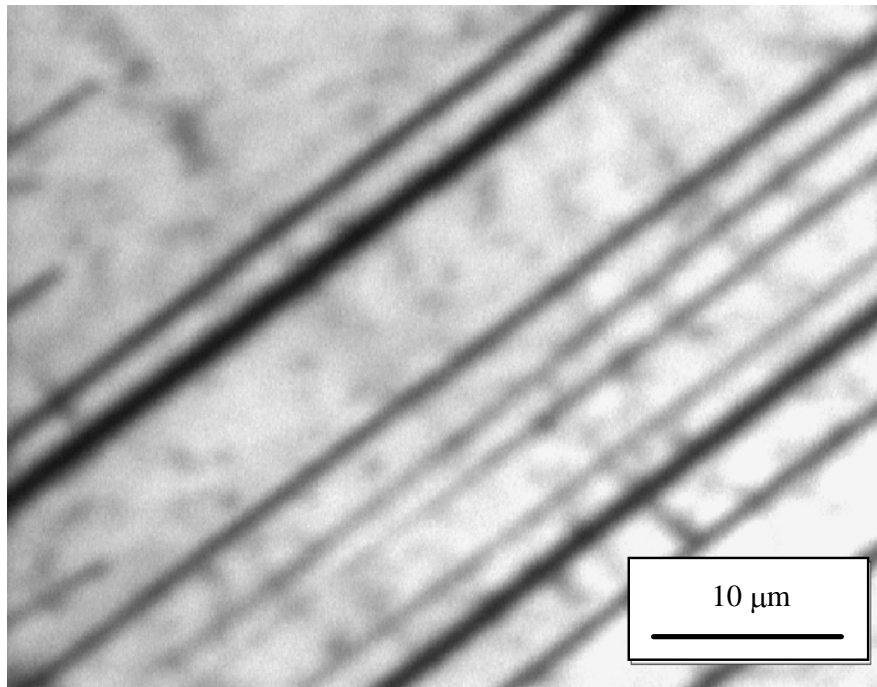


Figure 4.16a: Room temperature CL of $1\mu\text{m}$ ZnSe film grown by MBE on $4\mu\text{m}$ linearly graded (In,Ga)P buffer layer with a two minute Zn-exposed eight monolayer (2x4)-reconstructed GaAs layer between the (In,Ga)P and ZnSe (sample 11). Mag=1700x.

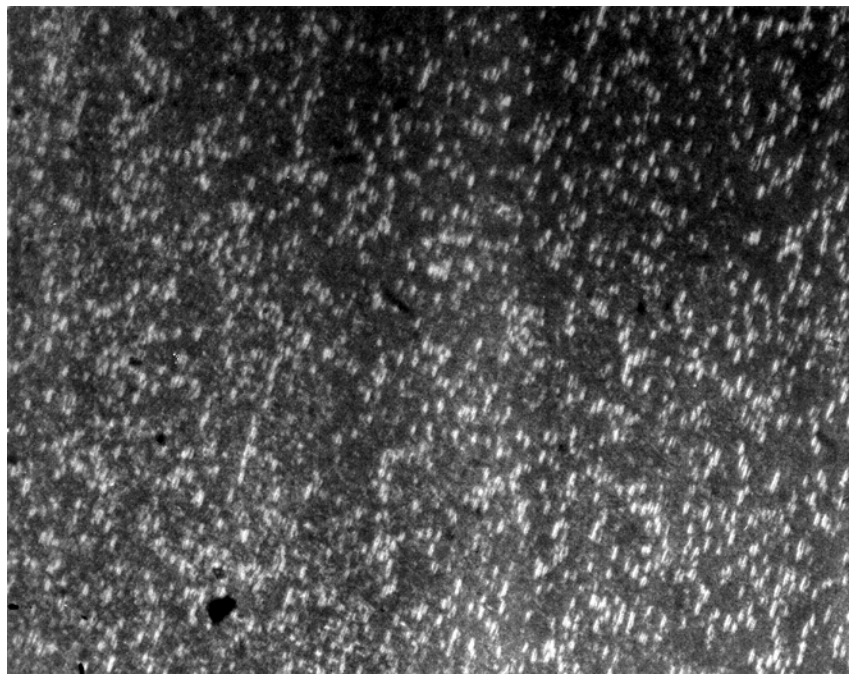


Figure 4.16b: EPD photograph of $1\mu\text{m}$ ZnSe film grown by MBE on $4\mu\text{m}$ linearly graded (In,Ga)P buffer layer with a two minute Zn-exposed eight monolayer (2x4)-

reconstructed GaAs layer between the (In,Ga)P and ZnSe (sample 11). $\text{Mag}=400\times$. $\text{EPD}=1.6\times 10^6 \text{ cm}^{-2}$.

the fully strained pseudomorphic GaAs cap layer or from the relaxed III-V/III-V buffer layer [45].

To further characterize these samples, AFM was performed. These results are shown in figure 4.17. The AFM plots show that ZnSe grown on the (2x4)-reconstructed GaAs surface results in a much smoother ZnSe layer ($R_a \sim 3\text{A}$) as compared to ZnSe grown on the c(4x4)-reconstructed GaAs surface ($R_a \sim 7\text{A}$).

MEE was also performed on a sample with the same structure as sample 11. A one minute Zn pre-exposure was performed, followed by forty cycles of MEE at the growth temperature. The CL and AFM images from this sample looked very similar to the samples grown by MBE.

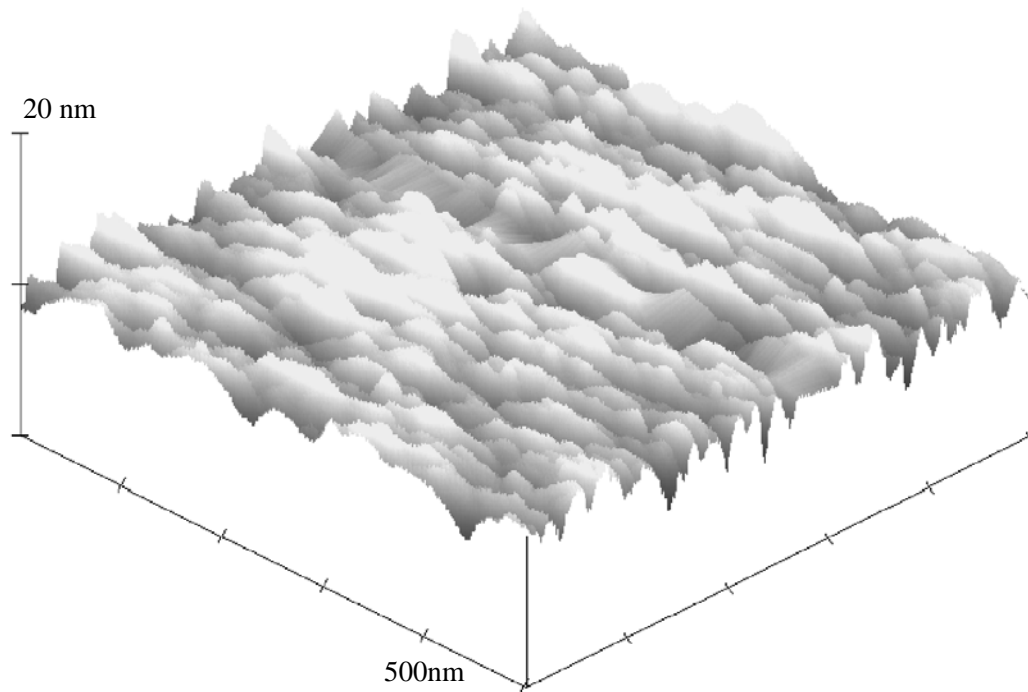


Figure 4.17a: Atomic force micrograph of $1\mu\text{m}$ ZnSe film grown by MBE on $4\mu\text{m}$ linearly graded (In,Ga)P buffer layer with a Zn-exposed 8 monolayer c(4x4)-reconstructed GaAs layer between the (In,Ga)P and the ZnSe (sample 10). $R_a = 7\text{A}$.

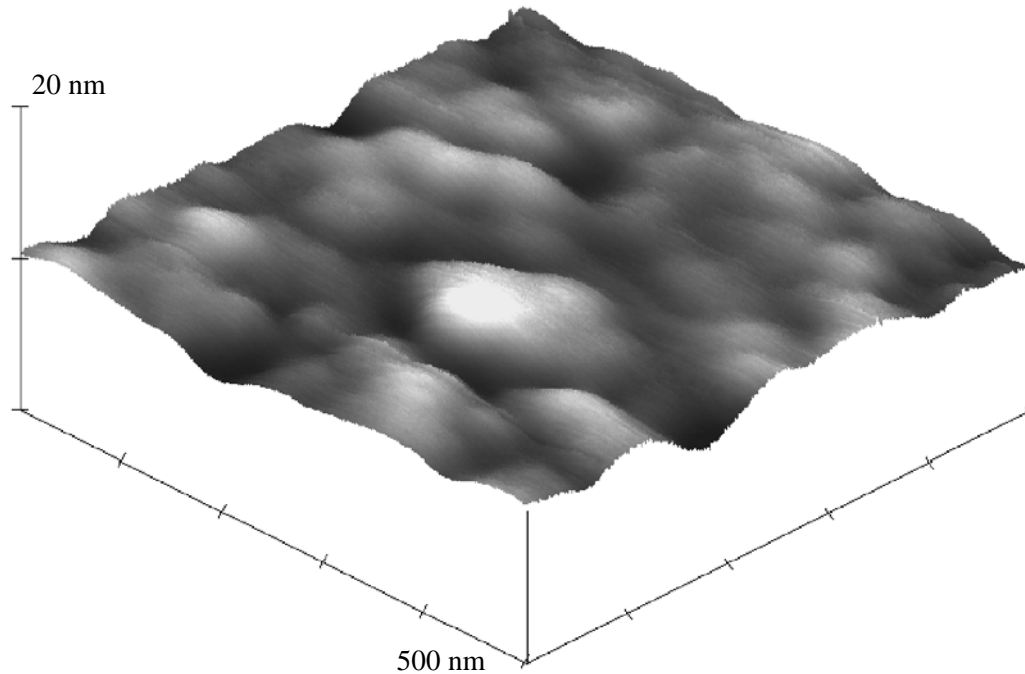


Figure 4.17b: Atomic force micrograph of 1 μ m ZnSe film grown by MBE on 4 μ m linearly graded (In,Ga)P buffer layer with a Zn-exposed 8 monolayer (2x4)-reconstructed GaAs layer between the (In,Ga)P and the ZnSe (sample 11). $R_a = 3\text{\AA}$.

4.4 Characterization by Photoluminescence

Another characterization technique that is widely used to prove that growth was of high quality is low temperature, 10K, photoluminescence. Photoluminescence (PL) is a sensitive, non-destructive technique for gaining an understanding of the optical properties of the semiconductor. Photoluminescence spectra displays the energies of the radiative recombination of photogenerated pairs, which are created by illumination above the bandgap of the material (see appendix).

Photoluminescence scans of each sample were taken to verify the correlation of defect density with nucleation. Figure 4.18 shows the PL spectra of the two samples consisting of 1 μ m ZnSe grown on a GaAs buffer layer with a Zn pre-exposure. In the

first case (figure 4.18a) the GaAs displayed a c(4x4) reconstruction, and, in the second (figure 4.18b), the GaAs displayed a (2x4) reconstruction.

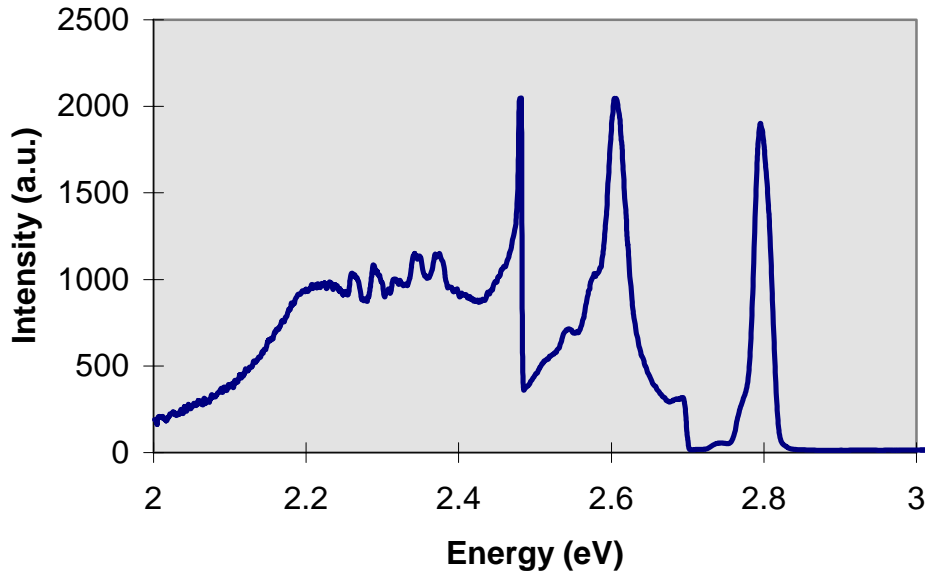


Figure 4.18a: 10K photoluminescence scan of 1 μ m ZnSe grown with a Zn pre-exposure on c(4x4)-reconstructed GaAs (sample 7).

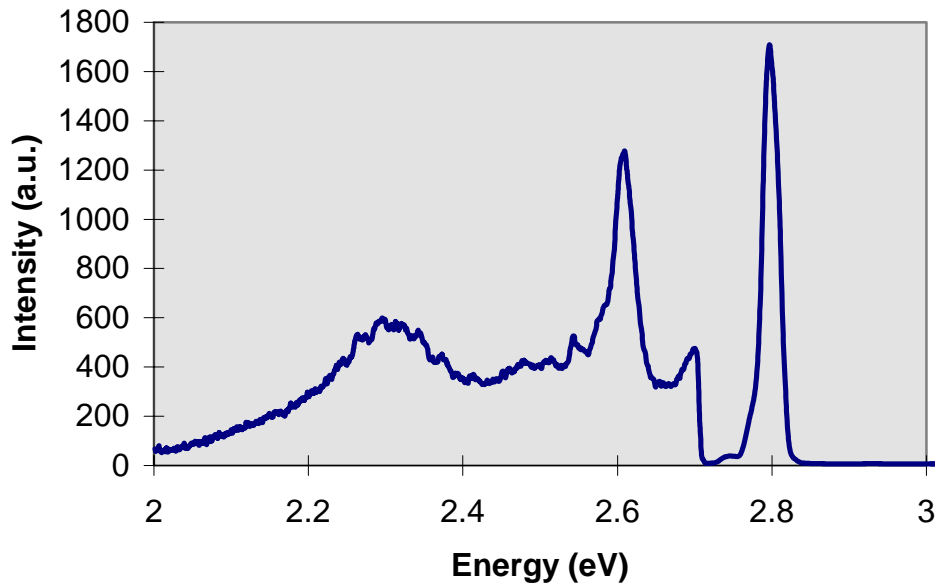


Figure 4.18b: 10K photoluminescence scan of 1 μ m ZnSe grown with a Zn pre-exposure on (2x4)-reconstructed GaAs (sample 9).

The large peak around 2.8 eV is the free exciton feature, DX; the peak around 2.6 eV is Y_0 ; the broad peak around 2.3 eV is a deep level band. The Y_0 feature has been correlated to extended structural defects [46], as has the deep level band. By normalizing the Y_0 intensity with the DX intensity, the variation in the DX intensities from sample to sample can be factored out, allowing for comparison among samples, shown in table 4.3.

Sample	Y_0/DX	Deep Level/DX	DD (cm^{-2})
7	4.3×10^{-2}	6.1×10^{-3}	$> 10^7$
9	7.5×10^{-3}	3.4×10^{-3}	1×10^6

Table 4.3: Correlation between Y_0 and deep level transitions measured by 10K PL, and dislocation density, DD (cm^{-2}), measured by CL and EPD, of samples 7 and 9.

As seen in table 4.3, higher defect densities resulted in higher normalized intensities of the Y_0 and deep level PL features. Thus, PL is consistent with the previous theory that MBE growth of ZnSe on (2x4)-reconstructed GaAs results in fewer dislocations than grown on c(4x4)-reconstructed GaAs.

PL measurements were also performed on samples 10 and 11, which incorporated graded layers of lattice-matched (In,Ga)P. Sample 10 had a thin capping layer of c(4x4)-reconstructed GaAs; sample 11 had a thin capping layer of (2x4)-reconstructed GaAs. The PL spectra are shown in figure 4.19.

Again, a normalized comparison of the PL defect levels is shown in table 4.4.

Sample	Y_0/DX	Deep Level/DX	DD (cm^{-2})
10	6.3×10^{-2}	5.1×10^{-3}	3×10^7
11	1.2×10^{-2}	3.3×10^{-3}	2×10^6

Table 4.4: Correlation between Y_0 and deep level transitions measured by 10K PL, and dislocation density, DD (cm^{-2}), measured by CL and EPD, of samples 10 and 11.

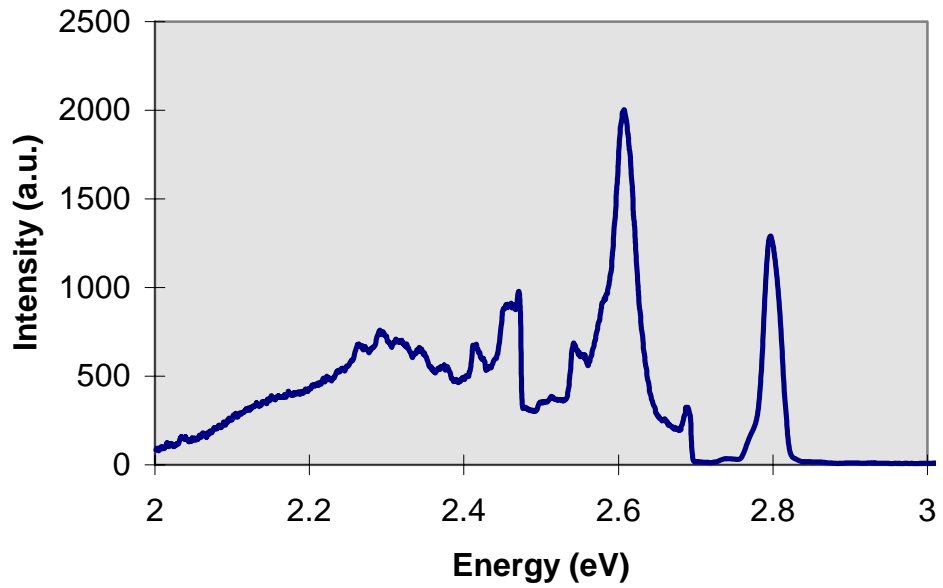


Figure 4.19a: 10K photoluminescence scan of $1\mu\text{m}$ ZnSe grown with a Zn pre-exposure on a graded (In,Ga)P buffer layer with a c(4x4)-reconstructed GaAs cap (sample 10).

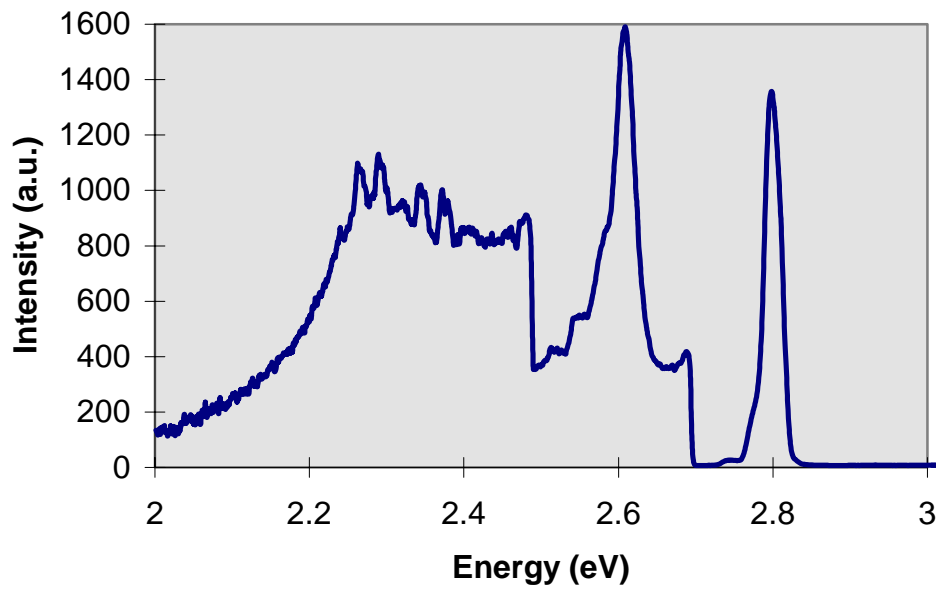


Figure 4.19b: 10K photoluminescence scan of $1\mu\text{m}$ ZnSe grown with a Zn pre-exposure on a graded (In,Ga)P buffer layer with a (2x4)-reconstructed GaAs cap (sample 11).

As can be seen from table 4.4 and from the PL spectra, sample 11 (ZnSe grown on graded (In,Ga)P with a (2x4)-reconstructed GaAs cap) has a lower defect density than sample 10 as well as lower normalized intensities of the Y_0 feature and the deep level band as measured by 10K PL. This data strengthens the previous result that growth of ZnSe on (2x4)-reconstructed GaAs yields fewer dislocations in the ZnSe epilayer than ZnSe growth on a c(4x4)-reconstructed GaAs surface.

Chapter 5: Future Research

5.1 LED Structure: Design and Analysis

As discussed, the ultimate goal of this research is to develop a light emitting diode with a III-V ohmic contact using a graded layer of (In,Ga,Al)P.

Thus far, the only tested device has been a standard pn diode consisting of ZnSe grown directly on c(4x4)-reconstructed GaAs without a pre-exposure of Zn or Se. Figure 5.1 schematically shows the design of the diode.

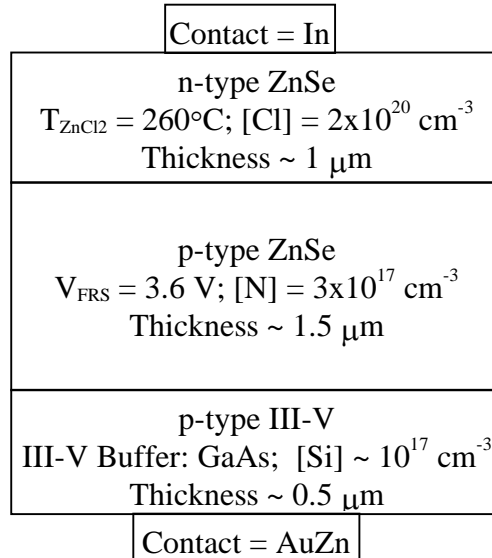


Figure 5.1: Schematic of pn diode showing doping and composition of each layer.

The threshold voltage of this pn diode, determined from the I-V plot in figure 5.2, is approximately 20 V. This is a very large value for such a device and must be significantly reduced. However, the large threshold was expected for this device. There is a 1 eV valence band offset between the ZnSe and the GaAs, which was not minimized in this case by the insertion of a III-V buffer layer with an intermediate bandgap energy.

Also, the ZnSe was simply grown on a c(4x4)-reconstructed GaAs surface, which has been shown to result in a significantly more dislocated epilayer than growth on (2x4)-reconstructed GaAs.

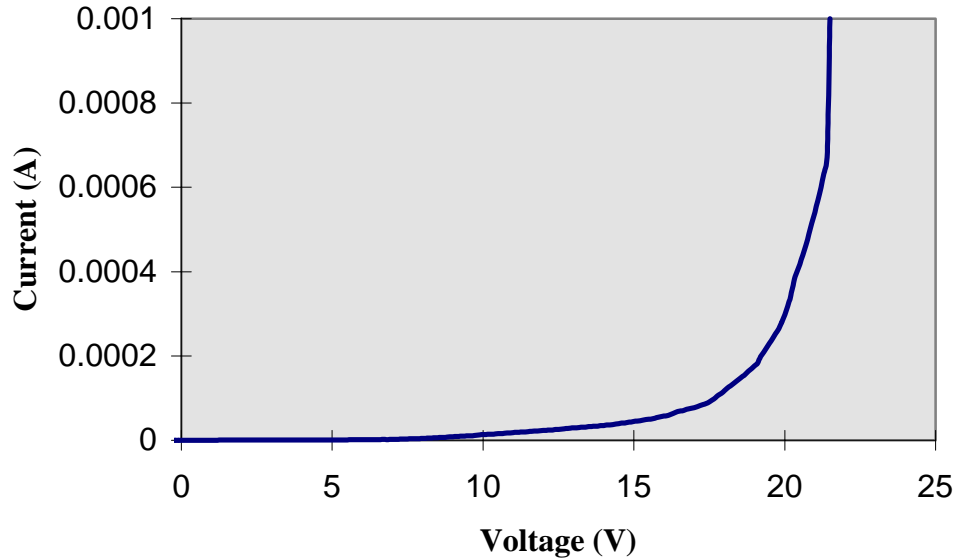


Figure 5.2: Current versus applied voltage characteristic of a ZnSe p-n diode consisting of ZnSe grown on c(4x4)-reconstructed GaAs.

In comparison, the 100 hour laser diode achieved by Sony Corporation had a threshold voltage of about 8 V with a defect density on the order of $3 \times 10^3 \text{ cm}^{-2}$ [8]. The diode described here had a threshold voltage of about 20 V with a defect density greater than 10^7 cm^{-2} .

5.2 Recent Advances

As discussed in the previous section, the nucleation technique used in the growth of ZnSe on GaAs plays a significant role in the quality of a ZnSe-based LED. It is for this reason that the greater part of this research focused on nucleation techniques. These studies have demonstrated that ZnSe grown on (2x4)-reconstructed GaAs (75% As

surface coverage) has a lower defect density than that of ZnSe grown on c(4x4)-reconstructed GaAs (100% As surface coverage) [38]. This nucleation can also be used for a lattice-matched III-V buffer layer, by first growing a thin, pseudomorphic, layer of (2x4)-reconstructed GaAs on the III-V buffer layer. These conclusions are based on a variety of characterization measurements, most notably cathodoluminescence, etch pit density measurements, and atomic force microscopy.

5.3 Future Pursuits

The next stage of research will involve the electrical characterization of the optimized growth of ZnSe/(2x4)-reconstructed GaAs, with a variety of III-V buffer layers. Assumedly, the threshold voltage of a ZnSe LED grown on (2x4)-reconstructed GaAs will have a lower threshold voltage than the LED discussed above. If this is the case, the threshold voltage will more precisely reflect the effects of varying degrees of valence band offset. Ideally, a low-threshold voltage ZnSe LED may be realized by using an optimized nucleation technique to grow ZnSe on a lattice-matched (In,Ga,Al)P III-V buffer layer with a low valence band offset to ZnSe.

APPENDIX

Appendix A: In-Situ Characterization Techniques

A.1 Reflection High Energy Electron Diffraction (RHEED)

An *in-situ* RHEED apparatus, located within the MBE chamber, is used to determine if growth is proceeding as expected. The apparatus consists of a high energy beam of electrons (5-40keV) directed at a low angle (2°) to the surface of the material [47]. Given these conditions, the de Broglie wavelength of these electrons is such that the penetration is low. Thus, the diffraction pattern is the result of the arrangement of the atoms on the surface of the layer.

The RHEED diffraction pattern yields information on the smoothness of the material's surface. Spot-like diffraction is due to the diffraction of the electron beam by a three-dimensional lattice (a rough surface). A smoother, two-dimensional lattice from a surface is characterized by a streaky RHEED diffraction pattern.

The surface reconstruction can also be determined. The reconstruction of the top layer is described by $(a \times b)$, where a and b indicate that the unit cell on the surface is $a \times b$ larger than that of the bulk crystal. Each reconstruction is characterized by a different RHEED pattern. The number of RHEED beams observed on the RHEED screen depends on the azimuthal direction of the electron beam. From this information, the ratio of the elements on the surface of the semiconductor is determined. For instance, for ZnSe, a (2×1) surface reconstruction occurs when the surface is Se-rich. A $c(2 \times 2)$ surface reconstruction occurs when the surface is Zn-rich. These surface reconstructions are shown below.

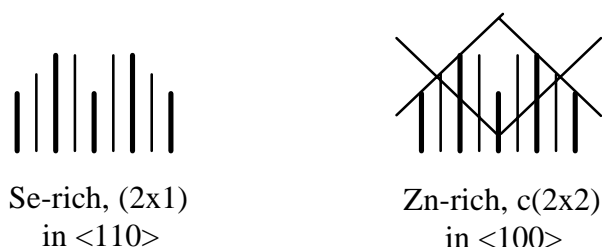


Figure A.1: ZnSe surface reconstructions for the Se-rich and Zn-rich cases.

RHEED oscillations at the onset of growth are also used to characterize the growth. When growth is initiated, the intensity of RHEED features is oscillatory. Each consecutive peak is due to the completion of a new monolayer. Thus, a measure of the number of peaks that occur in a known amount of time yields the growth rate. A lack of oscillations is often a warning of poor surface morphology.

A.2 Auger Electron Spectroscopy

The Auger electron spectroscopy (AES) technique for analysis of the surface composition of a compound is based on the process of Auger electron emission. As shown below [34], Auger electrons are generated when a focused beam of high energy electrons (20-5000eV) bombards the surface of the compound.

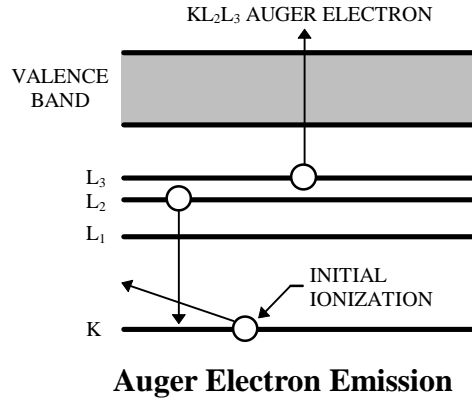


Figure A.2: Schematic of the theory of Auger electron emission.

Auger emission requires three electrons. Hence, elements with fewer than three electrons cannot be detected by AES. When an incident electron hits the surface (top 50Å) of a solid, an electron is emitted from the K-shell of an atom in the compound. An electron from the L₂ level of the atom then relaxes into the K-shell, which results in the emission of a photon. Sometimes, this photon will then drop to the L₃ level of the atom, causing the emission of an Auger electron.

The Auger electron is emitted with energy E_A , given by

$$E_A = E_K(Z) - E_{L_1}(Z) - E_{L_2}(Z + \Delta) - \Phi, [47]$$

where Z is the atomic number of the atom, Φ is the workfunction of the surface, and Δ is due to the charged state of the atom when the electron is in the L₂ level.

Each element of the periodic table emits Auger electrons at characteristic energies. The most intense Auger emissions are due to the KLL, LMM, and MNN transitions because electronic interactions are strongest among electrons in adjacent shells. Characterization of a compound is accomplished by comparing the energies of the Auger emission from a particular sample to a library of AES scans from standards, which show the principal Auger electron energies of each element of the periodic table (beginning with Lithium, element 3) for each of the three different Auger processes.

For quantitative measurements, the sensitivity of each element to the Auger emission process must be taken into account.

Appendix B: Structural Characterization

B.1 X-Ray Double Crystal Diffraction

X-Ray double crystal diffractometry (XRDCD) is a convenient post-growth technique used to determine the lattice mismatch between epitaxial layers. XRDCD can be performed immediately after growth with little preparation.

The XRDCD configuration has improved resolution over single crystal x-ray, because wavelength dispersion is eliminated [48]. XRDCD involves monochromatic x-rays of wavelength λ incident on a crystal. The rays will reflect from a plane of the crystal such that the reflected angle is equal to the incident angle, θ . Since each plane of the crystal is separated by its perpendicular lattice constant, d , the ray must travel an additional $2d\sin\theta$ to strike a subsequent plane.

From diffraction studies, two rays will be in phase when their path lengths differ by an integer number of wavelengths. From this comes Bragg's law:

$$2d\sin\theta_B = n\lambda, \text{ where } \theta_B \text{ is the Bragg angle.}$$

Epilayers may be effected by strain in two directions. d_{\perp} is the spacing between the lattice planes in the direction perpendicular to the layer surface and d_{\parallel} is the lattice spacing within the planes. When the x-ray diffraction is symmetric with respect to the surface, the reflection angle, θ_B , is determined only by d_{\perp} . Often, though, both d_{\perp} and d_{\parallel} are necessary to characterize the strain.

The strain of such a material may be determined by performing X-Ray analysis in two directions, represented by hkl . In this work, the (400) and (511) directions will be used. The (400) direction allows the determination of d_{\perp} . With this information, the (511) direction allows the determination of d_{\parallel} .

A material's diffraction peaks are mathematically related to its lattice constant by the equations below. $\Delta\theta$ is the difference in angle between the diffraction peak of the substrate and the layer. The substrate's lattice constant, d_{sub} , and its Bragg angles in both the (400) and (511) directions, $\theta_{B,400}$ and $\theta_{B,511}$, must be known.

$$\begin{aligned} d_{\perp} &= d_{\text{sub}} \sin(\theta_{B,400}) / \sin(\theta_{B,400} + \Delta\theta_{400}) \\ 2 \sin(\theta_{B,400}) (d_{\text{sub}}/4) &= 2 \sin(\theta_{B,511} + \Delta\theta_{511}) / [(h^2 + k^2)/d_{\parallel} + l^2/d_{\perp}]^{1/2} \end{aligned}$$

Finally, the relaxed lattice mismatch is determined by the strain components, d_{\parallel} and d_{\perp} , and by the materials' Poissons' ratio, ν . For the III-V buffer layers used in this research, ν is estimated to be 0.36.

$$(\Delta d/d)_{\text{relaxed}} = d_{\text{sub}} \{ [(1-\nu)/(1+\nu)][(d_{\perp}-d_{\text{sub}})/d_{\perp}] + [2\nu/(1+\nu)][(d_{\parallel}-d_{\text{sub}})/d_{\text{sub}}] + 1 \}$$

After growth, XRDCD was used in this research to determine whether the buffer layers were accurately grown with the desired lattice constants, and, in some cases, the amount of strain present in the sample.

B.2 Photoluminescence

Photoluminescence (PL) is a sensitive, non-destructive technique for measuring the optical properties of the semiconductor. Photoluminescence spectra displays the energies of the radiative recombination of photogenerated pairs, which are created by illumination above the bandgap of the material [49]. Typically, the spectra is generated when the sample is at cryogenic temperatures, in order to produce improved resolution and intensity of the output signal.

The primary features that are present in photoluminescence spectra are shown schematically below in figure B.1. The transitions observed are: CV, transitions from the conduction band to the valence band; X, free excitons; C^0X and A^0X , excitons bound to neutral donors and acceptors, respectively; CA, transitions from the conduction band to an acceptor; DA, transitions from donors to acceptors [47]. These recombinations are discussed in more detail elsewhere [50].

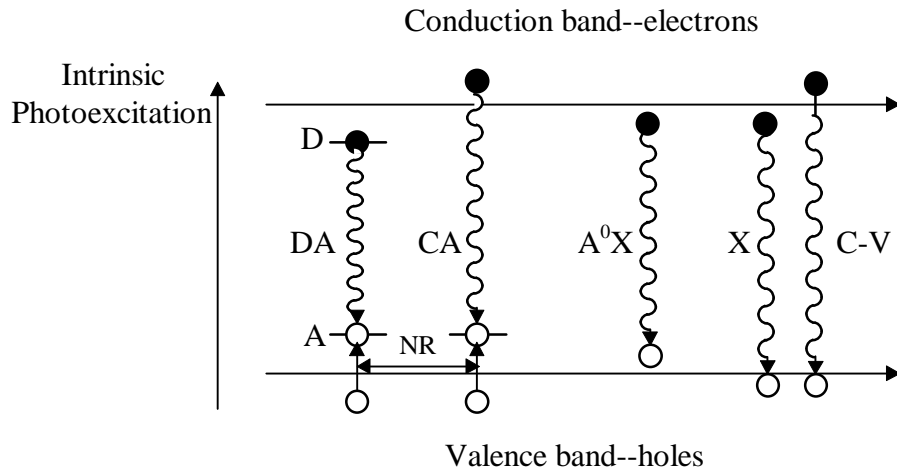


Figure B.1: Primary features seen in PL spectra of ZnSe epilayers.

B.3 Cathodoluminescence

Cathodoluminescence (CL) is a mode of scanning electron microscopy that produces materials characterization based on the emission of light due to electron bombardment. Theoretically, a cathodoluminescence spectra should yield similar results to that of a photoluminescence spectra.

Of greater interest than the luminescence spectra, is the microcharacterization of defects in semiconductors using cathodoluminescence. To image a sample by CL, first the energy of the electron beam is adjusted to determine the energy of maximum luminescence. Then, at that energy, the luminescence of the sample is imaged. In cathodoluminescence imaging of defects, contrast is generally due to the enhanced nonradiative recombination at dislocations in the crystal. Thus, it is possible to estimate the defect density.

Dislocation contrast appears as dots (due to threading dislocations) and as lines (due to misfit dislocations) [51]. Even further differentiation is due to the doping level. In lightly doped semiconductors, threading dislocations appear as very dark dots, with little contrast. Heavily doped semiconductors show hazier dots with greater contrast at these dislocation sites.

There are many difficulties making it impractical to rely on cathodoluminescence results for accurate determination of the defect density. One problem is that certain types of dislocations produce CL, while others do not [52]. Balk *et al.* reported contrast that is inversion likely due to localized heating effects at high beam currents, which may have led to the enhanced nonradiative recombination and a decrease in the CL signal [53]. However, in conjunction with other defect studies using Transmission Electron Microscopy (described below) or etch pit studies, CL imaging can be very enlightening.

B.4 Atomic Force Microscopy

Atomic Force Microscopy was developed in 1986 by G. Binnig *et al.* [54]. The instrument senses minute forces (10^{-12} - 10^{-8} N) between a sharp tip and the surface of a sample. AFM provides a method for non-destructive surface profilometry with atomic resolution. AFM relies on a small electrically conducting silicon cantilever, which bends due to the force exerted by the sample on the tip. The tip-to-sample distance is adjusted to maintain a constant cantilever deflection. In this way AFM is used to measure surface contours at very high resolution.

AFM was used in this research with a Digital 3000 Nanoscope in the tapping mode in air. Tapping Mode AFM was developed as a means of achieving high resolution without inducing destructive frictional forces. In tapping mode, the cantilever is oscillated near its resonant frequency as it is scanned over the sample surface. Contact with the sample results in a reduced oscillation amplitude, which allows the sample height to be calculated.

Surface morphology is sometimes characterized by the average roughness value (R_a) determined by AFM analysis. This value represents the average height of the sample.

B.5 Transmission Electron Microscopy

Transmission Electron Microscopy (TEM) is based on the diffraction of electrons through a very thin sample. The electron diffraction patterns seen in TEM imaging are spots for crystalline films, rings for randomly oriented films, and superimposed rings and spots from large grain polycrystalline films [47]. In terms of studying dislocations, TEM is the ideal technique. Each type of dislocation results in a different contrast effect that are seen in TEM images. These contrast effects, describe the extent of the various defects in a sample and give a precise means of determining defect density and a way of comparing a series of samples.

Perhaps the best use of TEM is that of cross-sectional analysis. This technique allows one to study each layer of a structure simultaneously. By studying the defects present in each layer, the origination point of the defects can be determined and the growth process can be systematically varied to better understand and to eventually reduce these defects.

Unlike the other characterization techniques discussed, TEM requires a complicated preparation process before the technique may be applied. It is also a destructive technique, such that the sample must first be thinned in a particular manner, making it unacceptable for any future use. The difficulty of preparation and the extensive time required make TEM a tedious characterization technique.

In order to improve the throughput and precision of the preparation of cross-sectional TEM samples, R. Anderson *et al.* from IBM recently developed the Tripod Polisher [55]. Cross sections of material specimens with few artifacts and a large area available for analysis can be prepared with this tool. The process involves mounting the specimen to the Tripod Polisher and mechanically polishing the specimen with progressively finer grit diamond films. The angle of the Polisher allows a wedge-shaped specimen to be prepared, which nearly eliminates the need for ion milling.

B.6 Etch Pitting

Etch pit characterization is a technique often used to reveal defects in solid materials. By slowing etching a solid with a specific etchant, pits can form at a point where dislocations intersect the solid surface. The pits are due to accelerated etching at dislocation sites. This technique has been discussed in great detail as a means of estimating defect density in solids [31]. Etch pit density (EPD) measurements do not necessarily reveal the precise dislocation density in a material, though. Etching often reveals point defects due to minute surface particles and other features not due to dislocations [36]. There is, however, significant evidence for a relationship between point defects and dislocations in semiconductors.

Bromine-methanol is the most common etchant for EPD studies of ZnSe-based materials. A correlation between the EPD found by this technique and the defect density as measured by TEM is well established. EPD measurements in this research were based on a one second etch of ZnSe in a 1% bromine solution of bromine-methanol at room temperature [56]. Such a one second etch removed 250 nm of ZnSe from the sample, revealing ovular pits at threading dislocations, as seen in figure B.2.

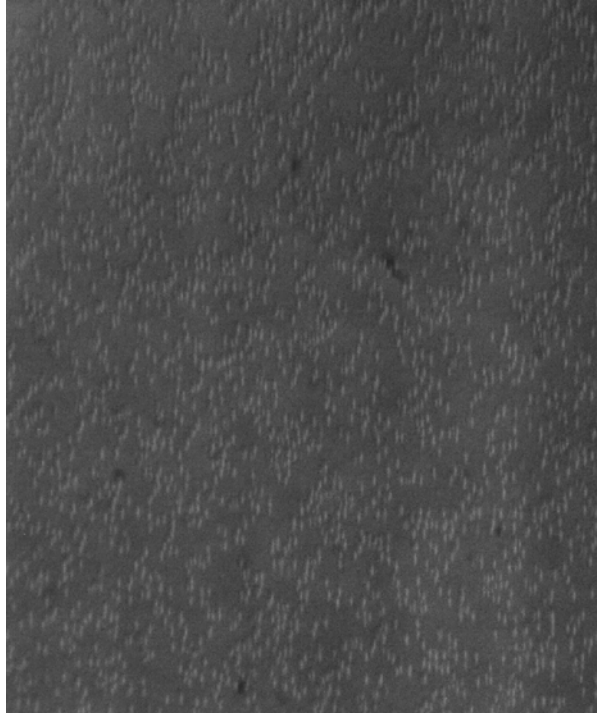


Figure B.2: Image of etch pits in sample of $1\mu\text{m}$ ZnSe/GaAs. One second etch with 1% bromine solution of bromine-methanol—250nm. EPD = $9 \times 10^7 \text{ cm}^{-2}$.

Appendix C Electrical Characterization

C.1 ZnSe pn-junction Diodes

Due to the current status of dopant capabilities of ZnSe, n^+p junction diodes are grown rather than p^+n diodes. Under forward bias, the current is determined by the number of electrons that can be injected into the p-type material. An applied voltage, V_A , positive at the p-type terminal of the pn-junction, reduces the potential drop across the barrier. This results in a lower barrier to diffusion and a lower drift field. Thus, more electrons and holes can cross the depletion region than in thermal equilibrium. This can be seen in figure C.1.

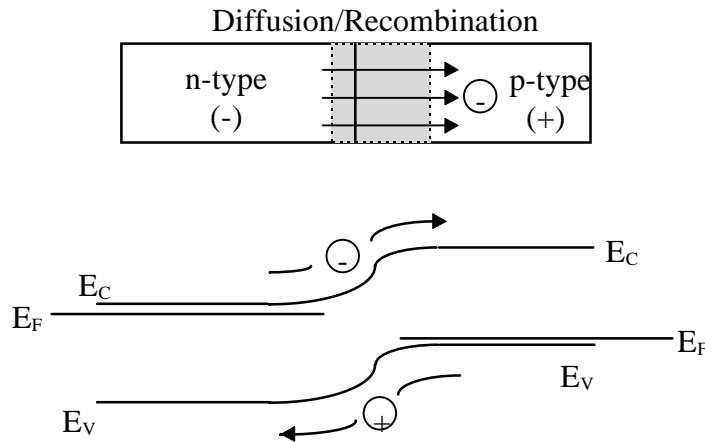


Figure C.1: Injection of electrons and holes under forward bias with $N_D \gg N_A$.

The concentration of holes in the n-region is negligible compared to the concentration of electrons in the p-region. Thus, to first order, the current is determined only by carriers injected from the heavily doped n-region to the more lightly doped p-region. The electrons diffuse and recombine as they cross the depletion region into the p-region. This forward current is described mathematically by the following relation.

$$J_F = J_0 \exp(eV_A/kT); \quad J_0 = (-eD_n n_i^2)/(L_n N_A)$$

D_n is the electron diffusion coefficient, L_n is the diffusion length of electrons, and n_i is the intrinsic concentration of electrons, N_A is Avogadro's number.

C.2 ZnSe Light-Emitting Diodes

Light-emitting diodes are fully described by the basic concepts of a forward biased pn-junction diode. By forward biasing the pn-junction, electrons injected from the n-type region to the p-type region recombine with holes in the p-type region, resulting in photon emission. To maximize the radiative recombination, a direct gap semiconductor

material is required. High-quality material is needed to minimize nonradiative recombination due to interface defects [57].

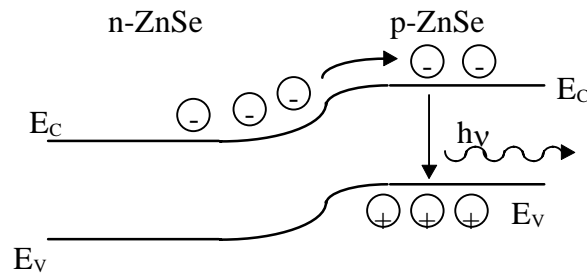


Figure C.2: Theoretical ZnSe LED with $N_D \gg N_A$.

A primary design constraint of LEDs is the need for a close lattice-match to the buffer layer to minimize misfit dislocations which have nonradiative centers and thus reduce injection.

C.3 I-V Measurements

In order for a pn-junction under forward bias to conduct current and emit light, carriers must be able to pass from one side of the junction to the other without recombining. It is this requirement that constrains the number of defects at the junction. A pn-junction diode has the property of rectifying alternating currents. The diode allows current to flow in only one direction. Figure C.3 shows a typical plot of the I-V characteristics of a II-VI semiconductor LED. The threshold voltage, V_T , marks the voltage in the forward direction required for large currents to begin to flow. I_r is the reverse leakage current, and V_r is the reverse breakdown voltage [58].

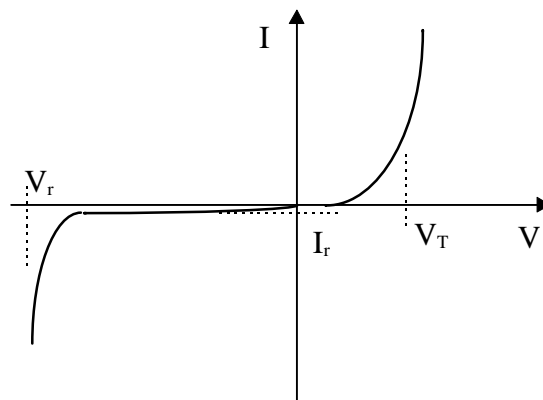


Figure C.3: General form of a current versus voltage characteristic for a p-n junction diode.

Optimally, the threshold voltage, the reverse breakdown voltage and the reverse leakage current are all low. By comparing I-V curves of different structures, electrical optimization can be obtained.

The first step in obtaining electrical measurements is to provide the sample with ohmic contacts. The formation of low resistance ohmic contacts is very important to the utility of a device, by allowing lower working voltages and lower power dissipation levels. The principles of ohmic contacts were established by Sze in the 1970s [50]. AuZn provides a good ohmic contact to p-type GaAs. A significant amount of research has been done to obtain a good ohmic contact to n-type ZnSe. Indium metal was first proposed in the 1960s [59]. Though it has somewhat low reliability due to its high contact resistance [60] and poor wetting [61], it can form an ohmic contact to n-ZnSe. Since this study simply required the ability to measure the relative threshold voltage and to correlate these values with the growth processes of the diodes, In served as the contact of choice. In order to attain a more accurate threshold voltage value, a structure was grown to measure the schottky voltage of n-ZnSe with In as the contact. Two microns of n-ZnSe were grown on n-GaAs. The n-GaAs was contacted with AuGe.

Ohmic contacts to the GaAs substrate were formed by evaporating the necessary metal in a thermal evaporator and annealing the metal in a rapid thermal annealer (RTA). The evaporation currents and the anneal times are given in Table C.1. To form Indium ohmic contacts on the n-ZnSe, the In was first etched by a solution of HCl:DiH₂O. The n-type ZnSe sample was then heated to 190°C and small pieces of indium were placed on the heated surface of the ZnSe for ten minutes to allow the metal to adhere to the semiconductor. The sample was then annealed in an RTA as described in table C.1.

Contact metal	Evaporation current	RTA Temperature	Anneal time
AuGe	15 A	420	10 sec
AuZn	15 A	375	30 sec
In	NA	250	10 min

Table C.1: Details of evaporation and thermal annealing for contacts to n-type and p-type GaAs and to n-type ZnSe.

Bibliography

- [1] T. Yao, *J. Cryst. Growth* **72** (1985) 31-40.
- [2] K. Ohkawa, T. Mitsuyu, and O. Yamazaki, "Low-resistivity Cl-doped ZnSe layers grown by molecular beam epitaxy," *Extended Abstracts of the 18th Conference on Solid State Devices and Materials, Tokyo*, (1986) 635.
- [3] R.M. Park, M.B. Troffer, C.M. Rouleau, J.M. Depuydt, and M.A. Haase, "P-type ZnSe by nitrogen beam doping during molecular beam epitaxial growth," *Appl. Phys. Lett.* **57** (1990) 2127-2129.
- [4] J. Qiu, J.M. DePuydt, H. Cheng, and M.A. Haase, "Heavily doped p-ZnSe:N grown by molecular beam epitaxy," *Appl. Phys. Lett.* **59** (1991) 2992.
- [5] M.A. Haase, J. Qiu, J.M. DePuydt, and H. Cheng, "Blue-green laser diodes," *Appl. Phys. Lett.* **59** (1991) 1272.
- [6] H. Jeon, J. King, W. Patterson, W. Xie, D.C. Grillo, M. Kobayashi, and R.L. Gunshor, "Blue-green injection laser diodes in (Zn,Cd)Se/ZnSe quantum wells," *Appl. Phys. Lett.* **59** (1991) 3619.
- [7] N. Nakayama, S. Itoh, K. Nakano, H. Okuyama, M. Ozawa, A. Ishibashi, M. Ikeda, and Y. Mori, "Room temperature continuous operation of blue-green laser diodes," *Electron. Lett.* **29** (1993) 1487.
- [8] S. Taniguchi, T. Hino, S. Itoh, K. Nakano, N. Nakayama, A. Ishibashi, and M. Ikeda, "100h II-VI blue-green laser diodes," *Electron. Lett.* **32** (1996) 552.
- [9] S. Nakamura, "Growth of $\text{In}_x\text{Ga}_{1-x}\text{N}$ compound semiconductors and high power InGaN/AlGaIn double heterostructure violet-light-emitting diodes," *Microelectronics Journal* **25** (1994) 269.
- [10] S. Nakamura, "A bright future for blue/green LEDs," *IEEE Circuits and Dev.* (May 1995) 19.
- [11] *Compound Semiconductor*, **1** (1995).
- [12] H. Amano, I. Akasaki, K. Hiramatsu, N. Koide, N. Sawaki, "Effects of the buffer layer in metalorganic vapour phase epitaxy of GaN on sapphire substrate," *Thin Solid Films* **163** (1988) 415.

- [13] H. Amano, M. Kito, K. Hiramatsu, I. Akasaki, "P-type conduction in Mg-doped GaN treated with low-energy electron beam irradiation (LEEBI)," *Japanese Journal of Applied Physics, Part 2* **28** (1989) L2112.
- [14] H. Amano, I. Akasaki, "GaN blue and UV light emitting diodes with a pn junction," *Oyo Buturi* **60** (1991) 163.
- [15] I. Akasaki, H. Amano, I. Suemune, "Recent progress of crystal growth, conductivity control and light emitters of column-III nitrides, and future prospect of nitride-based laser diode," *Proceedings of Silicon Carbide and Related Materials 1995* (1996) xxv+1120, 7-10.
- [16] N. Nakayama, S. Itoh, A. Ishibashi, Y. Mori, "High-efficiency ZnCdSe-ZnSSe ZnMgSSe green and blue light-emitting diodes," *Proc. SPIE - Int. Soc. Opt. Eng. (USA)* **2693** (1996) 36.
- [17] D.L. Barton, M. Osinski, C.J. Helms, N.H. Berg, B.S. Phillips, "Life tests and failure analysis of AlGaIn-InGaIn-GaN blue light emitting diodes," *Proc. SPIE - Int. Soc. Opt. Eng. (USA)*, (1996) **2693** 64.
- [18] R.L. Gunshor, A.V. Nurmikko, *MRS Bulletin*, (July 1995) 15.
- [19] J.W. Mayer, S.S. Lau, Electronic Materials Science: For Integrated Circuits in Si and GaAs (NY, MacMillan Publishing, 1990) page 431.
- [20] J. Reichow, J. Griesche, N. Hoffmann, C. Muggelberg, H. Rossmann, L. Wilde, F. Henneberger, and K. Jacobs, "MBE growth and characterization of ZnSe on GaAs," *J. Cryst. Growth*, **131**, 277-282.
- [21] M.B. Panish and H. Temkin, Gas Source Molecular Beam Epitaxy (Berlin, Springer Verlag, 1993) page 59.
- [22] E. Ho, *Growth and Doping of Zinc Selenide Using Alternative Gaseous Source Epitaxial Techniques*, Ph.D. thesis, Massachusetts Institute of Technology, June 1996.
- [23] G. Mandel, "Self-compensation limited conductivity in binary semiconductors, I. Theory," *Phys. Rev.* **134** (1964) A1073-A1079.
- [24] D.J. Chadi, K.J. Chang, "Self-compensation through a large lattice relaxation in p-type ZnSe," *Appl. Phys. Lett.* **55** (1989) 575.
- [25] K. Ohkawa, T. Karasawa, and T. Mitsuyu, "Characteristics of p-type ZnSe layers grown by molecular beam epitaxy with radical doping," *Jpn. J. Appl. Phys.* **30** (1991) L152-L155.
- [26] J. Qiu, J.M. De Puydt, H. Cheng, and M.A. Haase, "Heavily doped p-ZnSe:N grown by molecular beam epitaxy," *Appl. Phys. Lett.* **59** (1991) 2992.

- [27] S. Ito, M. Ikeda, and K. Akimoto, "Plasma doping of nitrogen in ZnSe using electron cyclotron resonance," *Jpn. J. Appl. Phys.* **31** (1992) L1316.
- [28] J. Petruzzello, B.L. Greenberg, D.A. Cammack, and R. Dalby, "Structural properties of the ZnSe/GaAs system grown by molecular-beam epitaxy," *J. Appl. Phys.* **63** (1988) p. 2299.
- [29] B.W. Dodson, "Work hardening and strain relaxation in strained-layer buffers," *Appl. Phys. Lett.* **53** (1988) p. 37.
- [30] H.C. Casey, Jr., M.B. Panish, Heterostructure Lasers, Part A, Fundamental Principles, Part B, Materials and Operating Characteristics, NY, Academic Press, 1978.
- [31] Hull, Derek, Introduction to Dislocation, NY, Pergamon Press, 1968.
- [32] H. Mitsuhashi, I. Mitsuhashi, M. Mizuta, and H. Kukimoto, "Coherent growth of ZnSe on GaAs by MOCVD," *Jpn. J. Appl. Phys.* **24**, L578 (1985).
- [33] J. Petruzzello, B.L. Greenberg, D.A. Cammack, and R. Dalby, "Structural properties of the ZnSe/GaAs system grown by molecular-beam epitaxy," *J. Appl. Phys.* **63** (1988) p. 2299.
- [34] S. Wolf and R.N. Tauber, Silicon Processing for the VLSI Era, CA, Lattice Press, 1986.
- [35] J. House, *Optical Characterization of ZnSe by Photoluminescence*, M.S. thesis, Massachusetts Institute of Technology, June 1994.
- [36] K. Shahzad, J. Petruzzello, D.J. Olego, D.A. Cammack, "Correlation between radiative transitions and structural defects in zinc selenide epitaxial layers," *Appl. Phys. Lett.* **57** 2452.
- [37] C.C. Chu, T.B. Ng, J. Han, G.C. Hua, R.L. Gunshor, E. Ho, E.L. Warlick, L.A. Kolodziejski, and A.V. Nurmikko, "Reduction of structural defects in II-VI blue green laser diodes," *Appl. Phys. Lett.* **69** (1996) 602.
- [38] D.K. Biegelsen, R.D. Bringans, J.E. Northrup, and L.-E. Swartz, "Surface reconstructions of GaAs(100) observed by scanning tunneling microscopy," *Phys. Rev. B.* **41** (1990) 41.
- [39] H. Yamaguchi, M. Kawashima, and Y. Horikoshi, "Migration-enhanced epitaxy," *Appl. Surf. Sci.* **33-34** 406 (1988).

- [40] R. Nicolai, *Phys. Rev. Lett.* **72** (1994) 294.
- [41] Z. Yu, S.L. Buczkowski, N.C. Giles, and T.H. Myers, "Hydrogenation of undoped and nitrogen-doped CdTe grown by molecular beam epitaxy," *Appl. Phys. Lett.* **69** (1996) 82.
- [42] D.K. Biegelsen, R.D. Bringans, J.E. Northrup, and L.-E. Swartz, "Surface reconstructions of GaAs(100) observed by scanning tunneling microscopy," *Phys. Rev. B.* **41** (1990) 5701.
- [43] J.M. Tartaglia, S.M. Crochiere, C.E. Kalnas, D.L. Farrington, J.A. Kronwasser, and P.J. Pearah, "A study of etch pit density and X-ray rocking curves for GaAs substrate evaluation," *J. Electron. Mater.* **20** (1991) 345.
- [44] C.H. Simpson and W.A. Jesser, "On the use of low misfit dislocation structures to filter threading dislocations in epitaxial heterostructures," *Phys. Stat. Sol. (a)* **149** (1995) 9.
- [45] E.L. Warlick, E. Ho, G.S. Petrich, L.A. Kolodziejcki, *J. Cryst. Growth*, *to be published*, 1997.
- [46] K. Shahzad, J. Petruzzello, D.J. Olego, D.A. Cammack, and J.M. Gaines, "Correlation between radiative transitions and structural defects in zinc selenide epitaxial layers," *Appl. Phys. Lett.* **57** (1990) 2452.
- [47] M.A. Herman and H. Sitter, Molecular Beam Epitaxy (Berlin, Springer-Verlag, 1989).
- [48] W.J. Bartels, J. Hornstra, and D.J.W. Lobeek, "X-ray Diffraction of Multilayers and Superlattices," *Acta Cryst.* **A42** (1986) 539.
- [49] M.B. Panish and H. Temkin, Gas Source Molecular Beam Epitaxy (Berlin, Springer-Verlag, 1993) p. 203.
- [50] S. M. Sze, Physics of Semiconductor Devices, John Wiley & Sons, New York, p. 36 (1981).
- [51] B.G. Yacobi, D.B. Holt, "Cathodoluminescence scanning electron microscopy of semiconductors," *J. Appl. Phys.* **59** R1 (1986).
- [52] G.R. Booker, A. Ourmazd, D.B. Darby, "Electrical recombination behaviour at dislocations in gallium phosphide and silicon," *J. Phys. Colloq.* **40** (1979) C6-19-21.
- [53] L.J. Balk, E. Kubalek, E. Menzel. (1976), "Investigations of as-grown Dislocations in GaAs Single Crystals in the SEM," in *Scanning Electron Microscopy/1976*, edited by O. Johari (SEM Inc., Chicago, IL), 257.

- [54] G. Binnig, C. F. Quate, and Ch. Gerber, "Atomic force microscopy," *Phys. Rev. Lett.* **12** (1986) p. 930.
- [55] J. Benedict, R. Anderson, S. Kleipis, "Recent developments in the use of the Tripod Polisher for TEM specimen preparation," *Mat. Res. Soc. Symp. Proc.* **254** 121 (1992).
- [56] Technique established based partly on discussions with T.B. Ng and R.L. Gunshor of Purdue University, July 1996.
- [57] J.W.Mayer, S.S.Lau, Electronic Materials Science: For Integrated Circuits in Si and GaAs (NY, MacMillan Publishing, 1990) 389.
- [58] D. A. Fraser, The Physics of Semiconductor Devices, Clarendon Press, Oxford, p. 59 (1986).
- [59] M. Aven, D.T.F. Marple, and B. Segall, *J. Appl. Phys. Suppl.* **32** (1961) 2261.
- [60] Y.X. Yang and P.H. Holloway, "Indium ohmic contacts to *n*-ZnSe,:" *AIP Conf. Proc.* **227** (1991) 134.
- [61] G.W. Ludwig and M. Aven, *J. Appl. Phys.* **38** (1967) 5326.